Postprint of: Skarżyński Ł., Tejchman-Konarzewski A., Investigations on fracture in reinforced concrete beams in 3-point bending using continuous micro-CT scanning, CONSTRUCTION AND BUILDING MATERIALS, Vol. 284 (2021), 122796, DOI: 10.1016/j.conbuildmat.2021.122796

Investigations on fracture in reinforced concrete beams in 3-point bending using continuous micro-CT scanning

Łukasz Skarżyński and Jacek Tejchman

Faculty of Civil and Environmental Engineering, Gdańsk University of Technology, Narutowicza Street 11/12, 80-233 Gdansk, Poland,

Email: lskarzyn@pg.edu.pl, tejchmk@pg.edu.pl

Abstract

This study explores a fracture process in rectangular reinforced concrete (RC) beams subjected to quasi-static three-point bending. RC beams were short and long with included longitudinal reinforcement in the form of a steel or basalt bar. The ratio of the shear span to the effective depth was 1.5 and 0.75. The focus was on the load-deflection diagram and crack formation. Three-dimensional (3D) analyses of the size and distribution of pores and cracks were carried out with an X-ray micro-computed tomography system SkyScan 1173 of high resolution that is a very valuable non-destructive tool for studying a 3D material interior. The tomography system was connected with a quasi-static loading machine ISTRON 5569 to continuously follow fracture changes without loading breaks. The beams failed in shear due to a diagonal shear crack that was steeper with basalt reinforcement. The shear strength and flexural strength of RC beams with steel reinforcement were higher by about 10% than of RC beams with basalt reinforcement. The deflection corresponding to the maximum load of RC beams was higher by about 20-25% in RC beams with basalt reinforcement due to its lower basalt modulus of elasticity. The final volume of cracks in beams reinforced with basalt bars was higher by about 9-20% than in concrete beams reinforced with steel bars due to a higher beam deflection whereas the maximum crack width in concrete beams reinforced with basalt bars was higher by about 20-40% than in concrete beams reinforced with steel bars. The critical shear crack in RC beams with basalt reinforcement was wider by about 20-40% and steeper by about 10-45% as compared to concrete beams with steel reinforcement. The relationship between the crack volume and beam deflection was bi-linear. Both, aggregate breakage and crack branching occurred during beam bending.

Keywords: X-ray micro-CT; continuous scanning; reinforced concrete; 3-point bending; shear failure; fracture

1. Introduction

Concrete is a dominant composite building material in the world in terms of volume that is widely used in the field of civil engineering due to easy fabrication and the lowest ratio between cost and strength as compared to other available materials. It possesses high compressive strength but both low tensile strength and ductility. Thus, it is vulnerable to cracks under static and dynamic loading which are a fundamental phenomenon in concrete materials [1]-[4]. At the mesoscopic level, concrete is a typical composite material consisting of multi-phases, including coarse and fine mineral aggregates, cement matrix, voids and interfacial transition zones (ITZs) between the aggregate and cement matrix. The diameter of coarse aggregate ranges from millimetres to centimetres whereas ITZs are only several dozen micrometres and the hydrated cement is few nanometres in width. Coarse aggregates with irregular shapes are randomly embedded in the mortar. Porous ITZs around aggregates are significantly weaker than aggregate and mortar and become attractors for a micro-crack propagation along aggregate boundaries. As a consequence, the concrete structures are strongly heterogeneous, demonstrating a non-linear stress-strain behaviour [5]-[7]. The assessment of the structural optimization and safety for quasi-brittle materials (like concrete) requires, however, a comprehensive understanding of the micro- and macro-cracking formation and propagation. Therefore, it is necessary to investigate a 3D meso-scale damage formation for evaluating the failure extent of materials.

Different experimental techniques have already been used to investigate a fracture process in quasi-brittle materials like concrete. Among the variety of techniques, the most popular are the scanning electron microscopy [8], [9], laser-spot [10], interferometry [11], [12], acoustic emission [13]-[15], neutron imaging [16] and X-ray micro-computed tomography (micro-CT) [17]-[32]. The use of X-ray micro-CT recently gained the highest popularity in reproducing and a better understanding of real 3D meso-structure of different cementitious materials. X-ray micro-CT enables to visualize and analyze quantitatively a shape and distribution of macro-pores, aggregate particles, fibres and cracks. Micro-CT may determine the 3D meso-structure inside the concrete material without destruction since different composition phases correspond to different X-ray absorption coefficients. Micro-CT images are collections of 2D grayscale images (the so-called slices) that are stacked digitally for revealing the entire 3D internal specimen structure. The smallest element of this 3D image is a voxel which possesses a grayscale value corresponding to the material density. The shortcomings of micro-CT concern both resolution and solid-phase separation capability. Our tomography system SkyScan 1173 has already been successfully used for observations of the

evolution of a concrete fracture process during three-point bending in plain concrete [18], [19], [29], tension splitting in plain concrete [21], uniaxial compression in plain concrete [22], compressive fatigue in plain concrete [23], It was also used in fibrous concrete with steel and basalt fibres [30]-[32]. The potential of micro-CT in concrete fracture propagation research was clearly demonstrated. The micro-CT images became an extremely valuable tool for constructing and validating numerical mesoscopic 2D and 3D models for concretes within continuum mechanics [33]-[39] and discrete mechanics [40]-[42]. Based on micro-CT images, we formulated a very realistic discrete element model for quantitative describing a fracture process in concrete under different loading types [18], [21], [22], [40]-[42].

The presented research work is experimentally oriented; it concerns reinforced concrete (RC) beams subjected to 3-point bending failing in shear. A combined high-resolution X-ray micro-computed tomography coupled with the quasi-static loading machine ISTRON 5569 was used for shorter beams. Such a system allowed us to capture 3D images of material meso-structure and fracture without the necessity to remove the load during scanning [29]. Thus, a crack closure due to unloading was avoided [29]. The images provided valuable information regarding the real distribution, shape, width and volume of macro-pores and cracks in RC beams. The micro-CT scanning started with an initial scan of non-cracked concrete beams and continued with scans made at 3 different loading points. For comparison purposes, the experiments were also performed with longer beams and two different types of reinforcement (steel or basalt reinforcement) to investigate the effect of both the beam size and reinforcement stiffness on the strength and fracture pattern of beams. The basalt reinforcement is made of volcanic rock basalt. It has some excellent properties such as high corrosion resistance, high tensile strength and low weight. It is resistant against alkali, acids, radiation and UV light, electromagnetic, electric and electrostatic indifference. It possesses high heat stability, environmental friendliness, non-toxicity, low water absorption and the same thermal expansion coefficient as concrete. The disadvantages of this reinforcement are the low elastic modulus, lack of yielding before rupture and low resistance to fire and shear. The compressive strength is lower by 20-50% than the tensile strength and static fatigue may occur. In addition, basalt bars are more expensive than traditional steel bars (ca. 4-5 times).

The current experimental study includes three novel elements: 1) detailed investigations of a complex 3D fracture process at the aggregate level in RC beams of different size and reinforcement type under quasi-static 3-point bending using micro-CT, 2) continuous scanning of a 3D fracture process in reinforced concrete beams under 3-point bending without their unloading and 3) determination of a relationship between the crack volume and beam deflection. The volume of pores

and cracks was determined in numbers for four different beam deflections. All beams did not include vertical shear reinforcement and hence failed in shear. Experimental results were compared with our other similar experimental outcomes on large RC beams using steel [43], [44] and basalt longitudinal reinforcement [43], [45] that also failed in shear. The micro-CT results in this paper may thus be used as a benchmark for numerical models to describe fractures in RC beams (e.g. [18], [21], [38], [40]). The micro-CT system has not been used for studying a fracture process in RC elements under mechanical loading yet in contrast to plain [46] and fibrous [31] concretes.

2. Experimental program for micro-CT

2.1 RC beam preparation

Concrete blocks were prepared from a mix including round-shaped aggregate particles with the mean diameter of d_{50}=2 mm and the maximum diameter of d_{max}=16 mm (Figure 1) with the addition of cement CEM I 32.5R and water. The water/cement ratio was w/c=0.42. A small amount of superplasticizer was added to improve the workability of the fresh concrete. The concrete mix components are presented in Table 1. Two cubic concrete blocks with the dimensions of 300×300×100 mm^3 reinforced with one steel or basalt bar of the diameter 6 mm were prepared. The basalt fiber content was 80% and the epoxy resin was 20%. The reinforcement ratio was always ρ=1.8%. The height of the ribs was 0.85 mm (steel bars) and 0.65 mm (basalt bars). The mechanical properties of reinforcement were as follows: the tensile strength of basalt f_{yb}=1100 MPa and steel f_{ys}=650 MPa and the modulus of elasticity of basalt E_b=70 GPa and steel E_s=200 GPa. For the first 7 days, the blocks were properly cured to eliminate the negative effect of autogenous shrinkage on planned test results [47]. Afterward, long (Figure 2) and short (Figure 3) rectangular reinforced concrete beams were cut out on the 28th day. All beams had the same cross-sectional dimensions, i.e. height h=40 mm and width b=40 mm. The effective height was D=30 mm (the concrete cover was 7 mm). The long beams had a length of L=160 mm and span of L_s=120 mm (L_s/D=3) and the ratio of a shear span and effective depth a/D=1.5. The short ones had a twice smaller length (L=80 mm), span (L_s=60 mm, L_s/D=1.5) and shear span ratio a/D=0.75. The dimensions of short beams were selected to be entirely visible in the field-of-view of our micro-CT system. The short beams were continuously scanned using the micro-CT equipment mounted on the Instron 5569 loading machine whereas the long beams were designated for scanning after the tests only. The average uniaxial compressive strength of concrete [48] was f_c=49.75 MPa with the standard deviation of 2.14 MPa (tested on 3 cubic concrete specimens 15×15×15 cm^3), the average Young's modulus [49] E=34.8 GPa with the standard deviation of 2.04 GPa and the average Poisson's ratio υ=0.21 with

the standard deviation of 0.02 (tested on 3 cylinder concrete specimens 15×30 cm^2). The mean tensile strength during bending was f_t=3.96 MPa [50] with the standard deviation of 0.22 MPa (tested on 3 concrete beams 60×15×15 mm^3). Due to a high value of ρ=1.8%, small ratio a/D=0.75-1.5<3 and lack of vertical reinforcement, a diagonal critical shear crack was expected to appear at the failure [43]-[45]. The laboratory tests were carried out with a displacement controlled option using the rate of 0.05 mm/min (long beams) and 0.002 mm/min (short beams).

2.2 X-ray micro-CT scanning

Since the beams of Figure 2 were too long to be inserted in an axial field-of-view, the usual scanning technique was used, i.e. the beams were scanned in a vertical position after a bending test was ended. The SkyScan 1173 scanner (Figure 4) was directly used for this usual scanning. The voltage and current were 130 keV and 61 μA. The scanning resolution resulted in a voxel size of 39 microns. The exposure time was settled on 5000 ms and the 0.2 mm brass filter was used. The beam was scanned at 360º with a single rotation step of 0.6º. The beams were scanned in two sub-scans by moving a rotation table down after the first sub-scan was completed. The reconstruction was made sub-scan by sub-scan with the necessary adjustment in file sequences to form a complete stack of the 3D volume.

For continuous scanning of short reinforced concrete beams of Figure 3, the SkyScan 1173 scanner was this time connected with the static Instron 5569 machine (Figure 5). To rotate loaded beams, a rotating table and stepper motor, controlled from the micro-CT software, were designed (Figure 5). The scanning process lasted 45 minutes. The voxel size was 46 microns and the exposure time was 3000 ms. The beam was scanned at 180º with a single rotation step of 0.6º.

The image reconstruction was carried out with the commercial software NRECON, CTAn and CTVox (Bruker microCT, Belgium). To reduce ring artifacts in reconstructed cross-sections, a random movement with the amplitude of 4 (number of camera lines) was used. To improve the image quality, the averaging option was set on 2 (number of frames). It averaged several images in each angular position. To distinguish pores, cracks and reinforcement from concrete on images, a careful threshold procedure based on density differences was performed (that is crucial for obtaining the material meso-structure from micro-CT scans). In our experiments, pores and cracks were separated from concrete with the threshold value in the range 0-70 whereas steel reinforcement with the threshold 230-255. The first threshold range value was validated, based on comparative measurement results of the air content in the concrete mass using the air pressure

method and porosity in concrete beams using micro-CT. The air content was 2.70%, 2.90% and 3.0% with an average value of 2.87% and the porosity was 2.64%, 3.04%, 2.67% and 2.83% with an average value of 2.79%. Both the average values were similar (which confirmed the threshold range value assumed in experiments). The basalt reinforcement could not be clearly distinguished from concrete due to the same density as the mortar. The pores were treated in two ways, i.e. as open pores that crossed the boundaries of VOI (volume of interest) or as closed pores that were entirely embedded in VOI. The volumes of pores (open, closed and total) and cracks were automatically measured. To calculate the actual crack volume, the volume of initial pores was subtracted from the actual volume of total pores.

3. Experimental micro-CT results for long RC beams

Figure 6 and Table 2 show the initial 3D content and distribution of-pores in non-cracked steel and basalt reinforced concrete beams measured by micro-CT. The initial volume of macro-voids in a non-cracked long concrete beam with a steel bar was 2.64% of the total beam volume (2.14% - closed pores and 0.50% - open pores) and with a basalt bar was 3.04% of the total beam volume (2.42% - closed pores and 0.62% - open pores). Thus, the total initial porosity of concrete beams with steel reinforcement was smaller by about 15% than the porosity of concrete beams with basalt reinforcement. Figure 6Ab shows that between steel bar ribs some free space was left. The free space was not observed between basalt bar ribs (Figure 6Bb).

Figure 7 presents the evolution of the vertical force F versus the deflection u for long concrete beams with a single steel and basalt bar subjected to three-point bending. The evolution of both curves was similar. The maximum vertical force of concrete beams with a steel bar was 4.77 kN and was higher about 10% than with a basalt bar - 4.35 kN. The deflection at the maximum force of the concrete beam with a steel bar, 0.57 mm, was about 25% smaller than with a basalt bar, 0.77 mm, due to the lower modulus of elasticity of basalt. The shear strength, $V=F_{max}/bD$, was 3.97 MPa (RC beam with a steel bar) and 3.62 MPa (RC beam with a basalt bar). The flexural strength, $M=1.5F_{max}\,L_s/bh^2$, was 13.48 MPa (RC beam with a steel bar) and 12.23 MPa (RC beam with a basalt bar). A double force peak occurred during deformation (which is typical in RC beams if the concrete cover is large enough [51]). After reaching both the peak values, the vertical force decreased. The beams' failure was brittle.

The crack development and failure mechanism were similar for concrete beams with two different reinforcement types. First, one (beam with a steel bar) or two flexural cracks (beam with a basalt bar) appeared at the area of the beam mid-span (that caused an initial jump on the force-deflection curve in Figure 7). Later, short inclined (shear) cracks developed in a shear span region that continuously evolved in length and width with increasing deflection. Next, one inclined dominant shear crack started to stronger develop. The failure took place in a rapid brittle way (independently of the reinforcement type) due to a diagonal critical shear crack at one beam side (the co-called shear-compression failure took place that is typical for the small ratios $a/D<2$ [45]) (Figures 8 and 9). The critical shear crack propagated from the bottom at the support region through the entire beam height up to the loading point. It propagated directly from the support at one side only (Figure 9) independently of the reinforcement type. On the other side, it was located at a certain distance from the support. Thus, a strongly non-symmetric shear-compression failure mode took place in beams. In addition, at the failure, a horizontal splitting macro-crack propagated from the critical shear crack along a basalt bar towards its end (Figures 9b and 10b). The bond between the concrete and steel bar was undamaged (Figure 10a). There existed, however, small cracks at each steel bar rib (Figures 8A and 10a). Just before the failure, some secondary cracks on the lateral sides of the beams also happened due to the bond damage (Figure 9). They appeared around the reinforcement bar on the beam lateral side with a steeper shear crack, being at a longer distance from the support (Figure 9). The crack volume in the concrete beam with steel reinforcement was 4.11% and basalt reinforcement was 4.52% (higher by 10%) after the test. The maximum crack width measured perpendicularly to the crack axis was 1.39 mm for the deflection u=1.05 mm in the RC beam with a steel bar and 1.68 mm (u=1.03 mm) with a basalt bar (Table 2). The final critical shear macro-crack was strongly curved and its shape and width varied along with the beam depth and height due to the heterogeneous nature of concrete (mainly due to the presence of aggregate particles different in shape and size) (Figures 8 and 9). The mean inclination of the critical shear crack to the bottom was 31^o (beam front) and 60^o (beam rear) for a steel bar and 43^o (front and rear side) for a basalt bar (Figure 8). The cracks mainly propagated through the cement matrix and ITZs around aggregates which were the weakest phase in concrete (Figure 11). Occasionally, the crack propagated through single weak aggregate particles (Figure 11). The crack branching also occurred during quasi-static bending (Figure 11). The greater the maximum crack width (connected with the higher crack volume) in the RC beam with basalt reinforcement was caused by a lower modulus of elasticity of basalt [33], [34].

4. Experimental micro-CT results for short RC beams

Figure 12 and Table 3 show the initial 3D content and distribution of pores in short non-cracked steel and basalt RC beams (L=80 mm) measured by micro-CT.

The initial volume of pores in a non-cracked short concrete beam with a steel bar was 2.67% of the total beam volume (the closed and open pores were 2.04% and 0.63%, respectively) and with a basalt bar was 2.83% of the total beam volume (the closed and open pores were 2.24% and 0.59%, respectively). The volume was again higher in the beam with a basalt bar (by about 5%).

The maximum vertical force of concrete with a steel bar 10.46 kN was about 15% higher than this with a basalt bar 9.05 kN (Figure 13). The shear strength for short beams, $V=F/bD$, was 8.72 MPa (steel bar) and 7.54 MPa (basalt bar) and for long beams 3.97 MPa (steel bar) and 3.62 MPa (basalt bar). Thus, it increased with decreasing a/D and L_t/D [45]. The flexural strength was 14.71 MPa (RC beam with a steel bar) and) and 12.73 MPa (RC beam with a basalt bar). It was higher by 5-10% than in long RC beams. The force-deflection diagram for short beams was slightly different than for long beams since a clear jump did not occur in the pre-peak region, softening after the peak load was more pronounced (in particular in the beam with a steel bar) and small re-hardening occurred in the beams after the peak load**.** The beams' failure was again brittle. The deflection corresponding to the maximum force was again higher (by about 20%) in the RC concrete with a basalt bar (0.33 mm) than in the RC beam with a steel bar (0.26 mm).

The RC beams were three times scanned by micro-CT for the different beam deflections: 1) close to the peak load (point '1' in Figure 13), 2) after the peak load in a softening regime (point '2' in Figure 13) and 3) close to the failure (point '3' in Figure 13). Figures 14a and 15a show the initial external view on the beam and the 3D distribution of pores from 2 different views. Figures 14b-d and 15b-d present images for the various loading points from 2 different views. The volume of pores in the non-cracked beams before the test was 2.67% and 2.83% for the RC beam with a steel and basalt bar, respectively (Table 3). At point "1" of Figure 13, the flexural cracks appeared in the beam span (Figures 14a and 15a) and the volume of pores and cracks increased by about 7.5% (beam with a steel bar) and by about 17% (beam with a basalt bar). The largest crack width for the concrete beam with a steel bar was w_{cs}=0.16 mm and with a basalt bar was w_{cb}=0.27 mm (higher by 60%). At point "2" of Figure 13, the first inclined (shear cracks) were observed (Figures 14b and 15b) and the volume of pores and cracks grew as compared to the point '1' by about 50% (beam with a steel bar) and by about 45% (beam with a basalt bar). The largest crack width in the concrete beam with a steel bar was w_{cs}=0.48 mm and in the concrete beam with a basalt bar was

w_{cb}=0.72 mm (higher by 35%). For point "3" of Figure 13, the inclined shear cracks evolved in length and width (Figures 14c and 15c) and the volume of pores and cracks increased as compared to the point '2' by about 40% for both the beams. The largest crack width in the RC beam with a steel bar was w_{cs}=1.25 mm and with a basalt bar was w_{cb}=1.78 mm (higher by 40%). Finally, the beam failure took place in a rapid brittle way in both RC beams due to a diagonal shear crack moving from the support region through a beam compressive zone towards the loading point. The critical shear crack in the RC beam with a steel bar propagated from the support to the loading point as the outermost crack (Figure 16) and in the beam with a basalt bar was situated closer to the mid-span of the beam at one side (front side). Similarly, as in long beams, some secondary cracks were visible on the lateral end sides of beams just before the beam failure. For a basalt bar (Figure 17b), the contact between concrete and a bar was again damaged at the failure - a horizontal splitting macro-crack propagated also along a basalt bar towards its end (similarly as in a long RC beam).

The mean inclination of the critical shear crack to the bottom was 59^o (front side) and 57^o (rear side) for the RC beam with a steel bar and 75^o (front side) and 50^o (rear side) for the RC beam with a basalt bar. The critical shear macro-cracks were steeper than in long beams due to a smaller ratio *a/D*. As compared to long RC beams, the final maximum width of cracks was smaller (by 10%) in the RC beam with a steel bar and larger (by 8%) in the RC beam with a basalt bar. The final crack volume was lower in short beams than in long beams by 25% (beams with steel reinforcement) and by 15% (beams with basalt reinforcement).

The change of the crack volume during bending is presented in Tables 4 and 5 and Figure 18. For comparison purposes, the final results shown in Figure 18 are also presented for long RC beams. A relationship between the crack volume and beam deflection (based on four micro-CT measurements) was bi-linear for both reinforcement types in short RC beams (Figures 18a and 18b). The final crack volume was about 3.3%-4.0% in short beams. It was slightly lower than in long RC beams (4.1%-4.5%, Figures 18c and 18d). The change of the curve inclination occurred at the peak load region where the crack volume was about 0.2-0.5%. For the deflection of u=1.0 mm, the crack volume was slightly lower in long beams assuming a continuous linear development of the crack volume in short beams between u=0.75-0.80 mm and u=1.0 mm.

The vertical cross-sectional micro-CT images in the beams (successively at 5 mm from the beam front side, at the beam mid-width and at 5 mm from the beam back side) of short concrete reinforced beams with steel or basalt reinforcement for the point '3' of Figure 13 are demonstrated in Figures 19 and 20. The crack width was measured perpendicularly to the crack axis and the

inclination angle was measured in relation to the horizontal line. The manual measurements were carried out in nine points. The shear crack width in the tensile region of the concrete beam reinforced with steel bar non-linearly changed with the beam height from w_{cs}=0.19 mm down to w_{cs}=1.25 mm (the average value was 0.61 mm with the standard deviation of 0.43 mm), whereas the inclination angle varied between α_s=26° and α_s=87° (the average value was 49° with the standard deviation of 25°). The shear crack width in the tensile region of the concrete beam reinforced with a basalt bar non-linearly changed with the beam height from w_{cb}=0.25 mm up to w_{cb}=1.78 mm (the average value was 1.08 mm with the standard deviation of 0.48 mm) whereas, the inclination angle varied between α_b=10° and α_b=96° (the average value was 54° with the standard deviation about 29°). It can be concluded (by taking into account the average values) that the critical shear crack in the concrete beam with basalt reinforcement was wider by about 75% as compared to the critical shear crack in the concrete beam with a steel bar. It was also steeper by about 10% on average. The crack propagated again sometimes through single weak aggregate particles. The crack branching also occurred.

The results in Sections 3 and 4 were shortly compared with our earlier experiments on large RC beams without vertical reinforcement during three- and four-point-bending) with steel reinforcement (h=200-800 mm, L=1500-6000 mm, a/D=1, ρ=1% [43], and h=200-400 mm, L=1500-3200 mm, a=480-2250 mm, a/D=1-3, ρ=1.4% [45]) and with basalt reinforcement (h=220-780 mm, L=400-1600 mm, a/D=3, ρ=0.63% [43], and h=200-1000 mm, L=1600-6000 mm, a/D=3, ρ=0.85% [44]). The strut-and-tie models following ACI [52] and Zhang and Tan [53] overestimated the shear strength of RC beams with steel reinforcement for a/h=1.5-2 (by 20%–100%) and underestimated for a/h=1 (by 5%–25%) [45]. The beams' behaviour with steel reinforcement was realistically described using a coupled elasto-plastic-damage model with non-local softening [54].

As compared to experiments on large beams with steel and basalt reinforcement, the crack development process and failure mode (shear-compression) were similar in the current study. The number of flexural and shear cracks was obviously significantly higher in large beams [43]-[45]. The beam deflections and the crack widths were also much higher when basalt reinforcement was used [43]. The bond damage occurred also in large RC beams with steel bars [43], [45]. The shear strength V in large RC beams was also higher with steel reinforcement than with basalt one [44]. For the same ratio a/D=1.5, the shear strength of large beams with steel reinforcement was V=2.86 MPa [45] and was thus lower by 40% than the shear strength of RC beams in Section 3 (V=3.97 MPa) due to a size effect caused by fracture [43].

The micro-CT experimental results constitute a reliable validation basis of numerical calculation outcomes with different mesoscopic continuous and discontinuous fracture models for concrete. They also provided some practical findings with respect to the 3D non-uniform cracks' shape due to the concrete heterogeneity, presence of voids along steel bar ribs in spite of careful concrete mixing, development of micro-cracks along steel bar ribs, the formation of secondary cracks in beams, propagation of a quasi-static macro-crack through weak aggregates in spite of low loads, crack branching during a quasi-static deformation process and quantitative evolution of the crack volume with concrete deformation.

5. Conclusions

In this study, experimental investigations of long and short RC beams with a steel or basalt bar under 3-point bending combined with a quantitative description of a fracture process using a continuous/discontinuous X-ray micro-computed tomography system (micro-CT) with high resolution were performed. The following findings can be offered:

- The shear strength and flexural strength of RC beams with steel reinforcement were higher by about 10% than those of RC beams with basalt reinforcement. The shear strength increased with decreasing ratios a/D and L_t/D. The shear strength of short RC beams was higher by 2.1-2.2 times than of long RC beams. The normalized shear strength normalized by the beam height was higher by 20% for short RC beams with a steel bar and by 10% for short RC beams with a basalt bar than for long beams. The deflection corresponding to the maximum load of RC beams was higher by about 20-25% in RC beams with basalt reinforcement due to its lower modulus of elasticity.

- The initial total porosity of non-cracked concrete beams reinforced with a steel bar (2.64-2.67%) was smaller by about 5-15% than of non-cracked concrete beams reinforced with a basalt bar (2.83-3.04%). Micro-CT images scanned before tests revealed the presence of voids along steel bar ribs in contrast to basalt bars.

- The beam bearing capacity was exhausted in a rapid brittle way through a diagonal critical shear crack that propagated from the bottom through the entire beam height up to the loading point (the so-called shear-compression failure occurred) connected with a horizontal splitting crack along a bar's end in RC beams with a basalt bar. Besides flexural and shear cracks, some secondary cracks

on beam lateral sides were created just before the failure due to bond damage. Short cracks also occurred at the ribs of steel bars.

- The final volume of cracks in beams reinforced with basalt bars was higher by about 9-20% than in concrete beams reinforced with steel bars due to a higher beam deflection. At the same time, the maximum crack width in concrete beams reinforced with basalt bars was higher by about 20-40% than in concrete beams reinforced with steel bars.

- The critical shear crack in short RC beams with basalt reinforcement was wider by about 40% and steeper by about 20% on average as compared to short concrete beams with steel reinforcement. For long RC beams, the critical shear crack was wider by about 20% when using basalt reinforcement (its mean inclination was similar). The inclination of the critical shear crack at both beam sides could strongly differ. The critical shear crack propagated from the support up to a loading point at one side only. It was the outermost crack in short beams with a steel bar while it was situated closer to the support than the outermost shear crack in short beams with a basalt bar.

- The final macro-crack was strongly curved and its shape and width varied along with the beam depth and height. The cracks mainly propagated through the cement matrix and ITZs. Sometimes, cracks moved through single weak aggregate particles. A crack branching phenomenon also occurred. The relationship between the crack volume and beam deflection was bi-linear (based on 4 scans for the different beam deflection). The final crack volume was 3.27-3.98% in short beams and 4.11-4.52% in long beams.

References

[1] A. Carpinteri, A.R. Ingraffea, *Fracture mechanics of concrete* (Martinus Nijhoff, ed.), The Netherlands, 1984.

[2] Z. Bažant, J. Planas, *Fracture and size effect in concrete and other quasi-brittle materials,* CRC Press LLC, Boca Raton, 1997.

[3] J.G.M. van Mier, *Fracture processes of concrete*. CRC press, 2017.

[4] J. Tejchman, J. Bobiński, *Continuous and discontinuous modelling of fracture in concrete using FEM*. Springer, Berlin-Heidelberg (eds. W. Wu and R. I. Borja), 2013.

[5] B. Pichler, C. Hellmich, Upscaling quasi-brittle strength of cement paste and mortar: A multi-scale engineering mechanics model, *Cement and Concrete Research*, 41 (2011), pp. 467-476.

[6] M. Königsberger, M. Hlobil, B. Delsaute, S. Staquet, C. Hellmich, B. Pichler, Hydrate failure in ITZ governs concrete strength: A micro-to-macro validated engineering mechanics model, *Cement*

412 *and Concrete Research,* 103 (2018), pp. 77-94.
413 [7] L. Skarżyński, J. Tejchman, Modeling the effect of material composition on the tensile
414 properties of concrete. Understanding the tensile properties of concrete (edited by Jaap Weerheijm).
415 *Woodhead Publishing Limited*, 48 (2013), pp. 52-97.
416 [8] T. Akçaoğlu, M. Tokyay, T. Çelik, Assessing the ITZ microcracking via scanning electron
417 microscope and its effect on the failure behaviour of concrete, *Cement and Concrete Research*,
418 35(2) (2005), pp. 358-363.
419 [9] J. Feiteira, E. Tsangouri, E. Gruyaert, C. Lors, G. Louis, N. de Beile, Monitoring crack
420 movement in polymer-based self-healing concrete through digital image correlation, acoustic
421 emission analysis and SEM in-situ loading, *Materials & Design*, 115 (2017), pp. 238-246.
422 [10] A. Scalbi, R. Olmi, G. Inglese, Evaluation of fractures in a concrete slab by means of laser-spot
423 thermography, *International Journal of Heat and Mass Transfer*, 141 (2019), pp. 282-29.
424 [11] J.A. Leendertz, Interferometric displacement measurement on scattering surfaces utilizing
425 speckle effect. *Journal of Physics E: Scientific Instruments*, 3 (1970), pp. 214–218.
426 [12] P .Jacquot, J.M. Fournier, Interferometry in Speckle Light: *Theory and Applications*. Springer,
427 Berlin, 2000.
428 [13] C. Chen, X. Fan, X. Chen, Experimental investigation of fracture behavior with different
429 loading rates based on acoustic emission, *Construction and Building Materials,* 237 (2020),
430 https://doi.org/10.1016/j.conbuildmat.2020.117472.
431 [14] S. Li, X. Fan, X. Chen, S. Liu, Y. Guo, Development of fracture process zone in full-graded
432 dam concrete under three-point bending by DIC and acoustic emission, *Engineering Fracture*
433 *Mechanics,* 230 (2020), https://doi.org/10.1016/j.engfracmech.2020.106972.
434 [15] D. Ren, B. Liu, S. Chen, D. Yin, M. You, H. Liou, L. Wu, Visualization of acoustic emission
435 monitoring of fracture process zone evolution of mortar and concrete beams under three-point
436 bending, *Construction and Building Materials*, 249 (2020),
437 https://doi.org/10.1016/j.conbuildmat.2020.118712.
438 [16] S. Roshankhah, J.P. Marshall, A. Tengattini, E. Ando, V. Rubino, A.J. Rosakis, G. Viggiani,
439 J.E. Andrade, Neutron imaging: a new possibility for laboratory observation of hydraulic fractures
440 in shale? *Géotechnique Letters,* 8 (2018), https://doi.org/10.1680/jgele.18.00129.
441 [17] T. Ponikiewski, J. Katzer, M. Bugdol, M. Rudzki, X-ray computed tomography harnessed to
2 determine 3D spacing of steel fibers in self compacting (SCC) slabs, *Construction and Building*
3 *Materials,* 74 (2015), pp. 102-208.
4 [18] Ł. Skarżyński, M. Nitka, J. Tejchman, Modelling of concrete fracture at aggregate level using
5 FEM and DEM based on X-ray micro-CT images of internal structure, *Engineering Fracture*
6 *Mechanics,* 147 (2015), pp. 13-35

447 [19] Ł. Skarżyński, J. Tejchman, Experimental investigations of fracture process in concrete by
448 means of X-ray micro-computed tomography, *Strain* 52(1) (2016), pp. 26-45.
449 [20] G.L. Balázs, O. Czobly, E. Lublóy, K. Kaplitány, A. Barsi, Observation of steel fibers
450 in concrete with Computed Tomography*, Construction and Building Materials,* 140 (2017),
451 pp. 534-541.
452 [21] J. Suchorzewski, J. Tejchman, M. Nitka, Experimental and numerical investigations of
453 concrete behaviour at meso-level during quasi-static splitting tension, *Theoretical and Applied*
454 *Fracture Mechanics*, 96 (2018), pp. 720-739.
455 [22] J. Suchorzewski, J. Tejchman, M. Nitka, DEM simulations of fracture in concrete under
456 uniaxial compression based on its real internal structure, *International Journal of Damage*
457 *Mechanics,* 27(4) (2018), pp. 578-607.
458 [23] Ł. Skarżyński, I. Marzec, J. Tejchman, Crack evolution in concrete compressive fatigue
459 experiments based on X-ray micro-CT images, *International Journal of Fatigue,* 122 (2018),
460 pp. 256-272.
461 [24] Q. Yu, H. Liub, T. Yang, H. Liu, 3D numerical study on fracture process
462 of concrete with different ITZ properties using X-ray computerized tomography*, International*
463 *Journal of Solids and Structures,* 147 (2018), pp. 204-222.
464 [25] C.M. Loeffler, Y. Qiua, B. Martin, W. Heard, B. Williams, X. Niea, Detection and
465 segmentation of mechanical damage in concrete with X-ray microtomography. *Materials*
466 *Characterization,* 142 (2018), pp. 515-522.
467 [26] M.A. Vicente, G. Ruiz, D.C. Gonzalez, J. Mínguez, M. Tarifa, X.X. Zhang, CT-Scan study of
468 crack patterns of fiber-reinforced concrete loaded monotonically and under low-cycle fatigue.
469 *International Journal of Fatigue,* 114 (2018), pp. 138-147.
470 [27] M.A. Vicente, J. Mínguez, D.C. Gonzalez , Computed tomography scanning of the internal
471 microstructure, crack mechanisms and structural behaviour of fiber-reinforced concrete under static
472 and cyclic bending tests, *International Journal of Fatigue,* 121 (2019), pp. 1-19.
473 [28] J.D. Ríos, C. Leive, M.P. Ariza, S. Seitl, H. Cifuentes, Analysis of the tensile fracture
474 properties of ultra-heigh-strength fiber-reinforced concrete with different types of steel fibers by
475 X-ray tomography, *Materials and Design,* 165 (2019), pp. 1-14.
476 [29] Ł. Skarżyński, J. Tejchman, Experimental investigations of damage evolution in concrete
7 during bending by continuous micro-CT scanning, *Materials Characterization,* 154 (2019) 40-52.
8 [30] Ł. Skarżyński, Mechanical and radiation shielding properties of concrete reinforced with
9 boron-basalt fibers using Digital Image Correlation and X-ray micro-computed tomography.
0 *Construction and Building Materials*, 255 (2020), https:
1 //doi.org/10.1016/j.conbuildmat.2020.119252.

[31] M. Miletić, L. Mohana Kumar, J.-Y. Arns, A. Agarwal, S.J. Foster, C. Arns, D. Perić, Gradient-based fibre detection method on 3D micro-CT tomographic image for defining fibre orientation bias in ultra-high-performance concrete. *Cement and Concrete Research*, 129 (2020), 105962.

[32] Ł. Skarżyński, J. Suchorzewski, Mechanical and fracture properties of concrete reinforced with recycled and industrial steel fibers using Digital Image Correlation technique and X-ray micro-computed tomography, *Construction and Building Materials*, 183 (2018), pp. 283-299.

[33] T.T. Nguyen, J. Yvonnet, M. Bornert, C. Chateau, Initiation and propagation of complex 3D networks of cracks in heterogeneous quasi-brittle materials: Direct comparison between in situ testing-microCT experiments and phase field simulations, *Journal of the Mechanics and Physics of Solids*, 95 (2016), pp. 320-350.

[34] Y. Huang, Y. Zhenjun, R. Wenyuan, G. Liu, C. Zhang, 3D meso-scale fracture modelling and validation of concrete based on in-situ X-ray Computed Tomography images using damage plasticity model, *International Journal of Solids and S*tructures, 67-68 (2015), pp. 340–352.

[35] Y. Huang, D. Yan, Z. Yang, G. Liu, 2D and 3D homogenization and fracture analysis of concrete based on in-situ X-ray Computed Tomography images and Monte Carlo simulations, *Engineering Fracture Mechanics*, 163 (2016), pp. 37-54.

[36] Z. Yang, W. Ren, R. Sharma, S. McDonald, M. Mostafavi, Y. Vertyagina, T.J. Marrow, In-situ X-ray computed tomography characterization of 3D fracture evolution and image-based numerical homogenization of concrete. *Cement and Concrete Composites*, 75 (2017), pp. 74-83.

[37] W. Trawiński, J. Bobiński, J. Tejchman, Two-dimensional simulations of concrete fracture at aggregate level with cohesive elements based on X-ray micro-CT images, *Engineering Fracture Mechanics,* 168 (2016), pp. 201-226.

[38] W. Trawiński, J. Tejchman, J. Bobiński, A three-dimensional meso-scale approach with cohesive elements to concrete fracture based on X-ray μCT images, *Engineering Fracture Mechanics,* 189 (2018), pp. 27-50.

[39] M. Khorman, V.R. Kalat Jaari, I. Aghayan, S.H. Ghaderi, A. Ahmadyfard, Compressive strength determination of concrete specimens using X-ray computed tomography and finite element method. *Construction and Building Materials,* 256 (2020), doi.org/10.1016/j.consbuildmat.2020.119427

[40] M. Nitka, J. Tejchman, A three-dimensional meso scale approach to concrete fracture based on combined DEM with X-ray μCT images, *Cement and Concrete Research,* 107 (2018), pp. 11-29.

[41] M. Nitka, J. Tejchman, Meso-mechanical modelling of damage in concrete using discrete element method with porous ITZs of defined width around aggregates, *Engineering Fracture Mechanics,* 231 (2020), 107029.

[42] M. Nitka, J. Tejchman, Comparative DEM calculations of fracture process in concrete considering real angular and artificial spherical aggregates, *Engineering Fracture Mechanics,* 239, (2020), 107309.
[43] E. Syroka-Korol, J. Tejchman, Experimental investigations of size effect in reinforced concrete beams failing by shear, *Engineering Structures,* 58 (2014), pp. 63-78**.**
[44] J. Suchorzewski, E. Korol, J. Tejchman, Z. Mróz. Experimental study of shear strength and failure mechanisms in RC beams scaled along height or length. *Engineering Structures,* 157 (2018), pp. 203-223.
[45] E. Korol, J. Tejchman, Z. Mróz, Experimental and numerical assessment of size effect in geometrically similar slender concrete beams with basalt reinforcement, *Engineering Structures,* 141 (2017), pp. 272-291.
[46] S.-Y. Chung, J.-S. Kim, D. Stephan , T.-S. Han, Overview of the use of micro-computed tomography (micro-CT) to investigate the relation between the material characteristics and properties of cement-based materials, *Construction and Building Materials*, 229 (2019), 116843.
[47] EN 12390-2:2009 Testing hardened concrete – Part 2: Making and curing specimens for strength tests.
[48] EN 12390-3:2009 Testing hardened concrete – Part 3: Compressive strength of test specimens.
[49] EN 12390-13:2013 Testing hardened concrete. Determination of secant modulus of elasticity in compression.
[50] EN 14651:2005+A1:2007 Test method for metallic fiber concrete. Measuring the flexural tensile strength (limit of proportionality (LOP), residual).
[51] Z. Bazant, J. Planas, *Fracture and size effect in concrete and other quasibrittle materials*. CRC Press, 1998.
[52] ACI 318-14: Building code requirements for structural concrete. American Concrete Institute; 2014.
[53] N. Zhang, K.H. Tan, Size effect in RC deep beams: Experimental investigation and STM verification, *Engineering Structures*, 29 (2007), pp. 3241-3254.
[54] I. Marzec, J. Tejchman, Z. Mróz, Numerical analysis of size effect in RC beams scaled along height or length using elasto-plastic-damage model enhanced by non-local softening, *Finite Elements in Analysis and Design*, 157 (2019), pp. 1-20.

LIST OF FIGURE CAPTIONS

Figure 1: Particle size distribution curve of concrete (mean particle diameter d_{50}=2 mm and maximum particle diameter d_{max}=16 mm, d - particle diameter)

Figure 2: Geometry of long concrete beam reinforced with one steel/basalt bar (dimensions are in [mm])

Figure 3: Geometry of short concrete beam reinforced with one steel/basalt bar (dimensions are in [mm])

Figure 4: Long reinforced concrete beam mounted vertically on rotation table of extended X-ray micro-CT SkyScan 1173 scanner

Figure 5: General view on X-ray micro-CT system Skyscan 1173 mounted on loading machine Instron 5569 and zoom on short reinforced concrete beam mounted on rotation table in horizontal position

Figure 6: Initial view on beams a) and distribution of pores in 3D micro-CT images b) of non-cracked long RC beams (L=160 mm) before loading: A) with steel bar and B) with basal bar

Figure 7: Experimental vertical force F - deflection u diagrams for long RC beams (L=160 mm) with: a) steel and b) basalt bar

Figure 8: Final 3D micro-CT images on 2 sides of long cracked concrete beams (L=160 mm) reinforced with: A) steel bar and (B) basalt bar for deflection about u=1.0 mm (a) beam front side and b) beam rear side, pores and cracks are in red, steel bar is in green)

Figure 9: Sketch of final crack pattern in long RC beams (L=160 mm) on all sides with: a) steel bar and b) basalt bar (cracks are marked in red, critical shear crack is marked as thick red line, reinforcement bar is marked in green)

Figure 10: Vertical cross-section at mid-width of long RC beam (L=160 mm) with: a) steel bar and b) basalt bar

Figure 11: Crack crossing weak aggregate and crack branching in long RC beam (L=160 mm) with: a) steel bar and b) basalt bar

Figure 12: General view on beams and distribution of pores in 3D micro-CT images of non-cracked short RC beams (L=80 mm) before loading reinforced with: a) steel bar and b) basal bar

Figure 13: Experimental force (F) deflection (u) curve for short RC beams (L=80 mm) with: a) steel bar and b) basalt bar and marked micro-CT scanning points '1'-'3'

Figure 14: 3D micro-CT images of short RC beam reinforced with steel bar (L=80 mm) on both sides for: a) point '1', b) point '2' and c) point '3' on curve F=f(u) of Figure 13 (pores and cracks are in red, steel bar is in green)

Figure 15: 3D micro-CT images of short RC beam reinforced with basalt bar (L=80 mm) on both sides for: a) point '1', b) point '2' and c) point '3' on curve F=f(u) of Figure 13 (pores and cracks are in red, steel bar is in green)

Figure 16: Sketch of final crack pattern for short RC beams (L=80 mm) on all sides with: a) steel bar and b) basalt bar (failure crack is marked as thick red line, reinforcement is marked in green)

Figure 17: Vertical cross-section at mid-width of short RC beam (L=80 mm) with: a) steel bar and b) basalt bar

Figure 18: Relationship between volume of cracks and deflection u during bending for RC beams: a) short beam with steel bar (L=80 mm), b) short beam with basalt bar (L=80 mm), c) long beam with steel bar (L=160 mm) and d) long beam with basalt bar (L=160 mm)

Figure 19: Vertical cross-sections of short RC beam (L=80 mm) with steel reinforcement: a) at 5 mm from front side, b) at beam mid-width and c) at 5 mm from rear side and corresponding measurement results of critical shear crack: d) crack width and e) crack inclination angle

Figure 20: Vertical cross-sections of short RC beam (L=80 mm) with basalt reinforcement: a) at 5 mm from front side, b) at mid-width and c) at 5 mm from rear side and corresponding measurement results of critical shear crack: e) crack width and f) crack inclination angle

LIST OF FIGURES

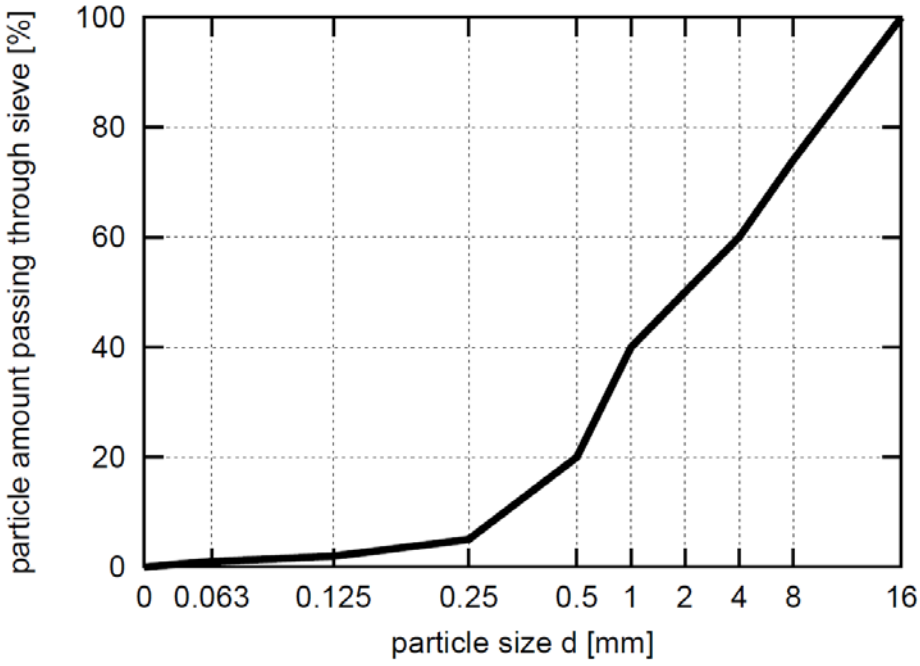

Figure 1: Particle size distribution curve of concrete (mean particle diameter d_{50}=2 mm and maximum particle diameter d_{max}=16 mm, d - particle diameter)

FIGURE 1

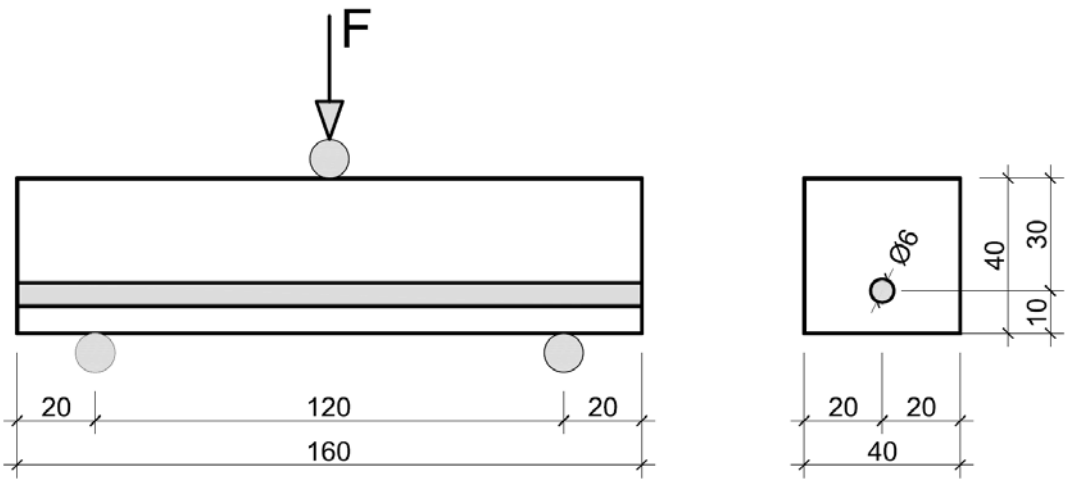

Figure 2: Geometry of long concrete beam reinforced with one steel/basalt bar (dimensions are in [mm])

FIGURE 2

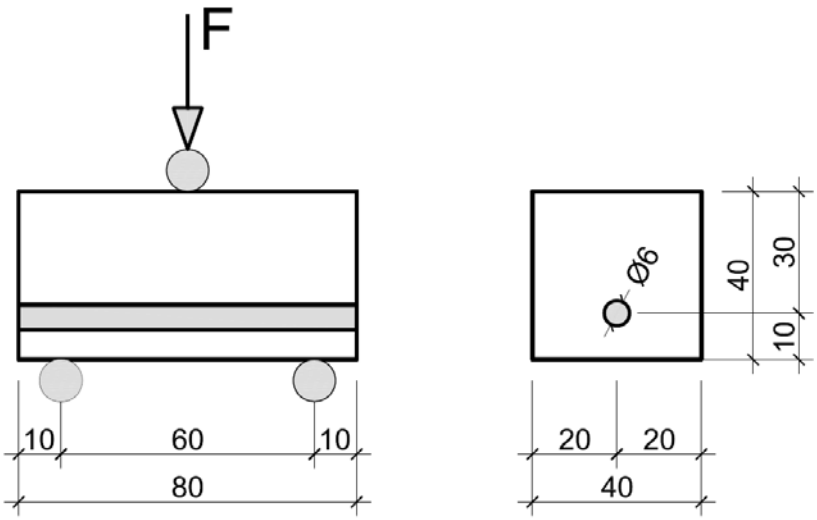

Figure 3: Geometry of short concrete beam reinforced with one steel/basalt bar (dimensions are in [mm])

FIGURE 3

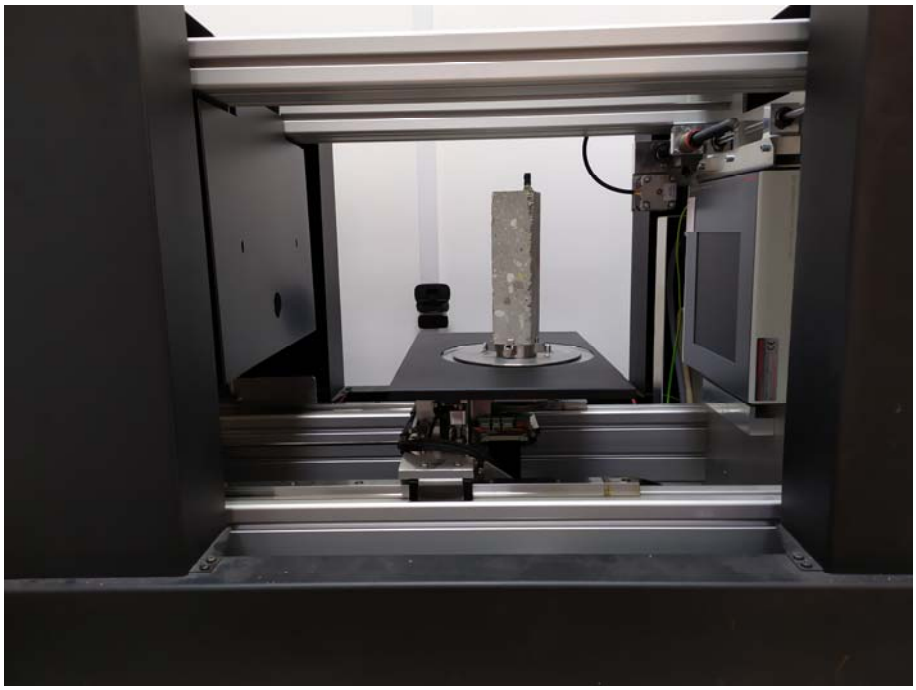

Figure 4: Long reinforced concrete beam mounted vertically on rotation table of extended X-ray micro-CT SkyScan 1173 scanner

FIGURE 4

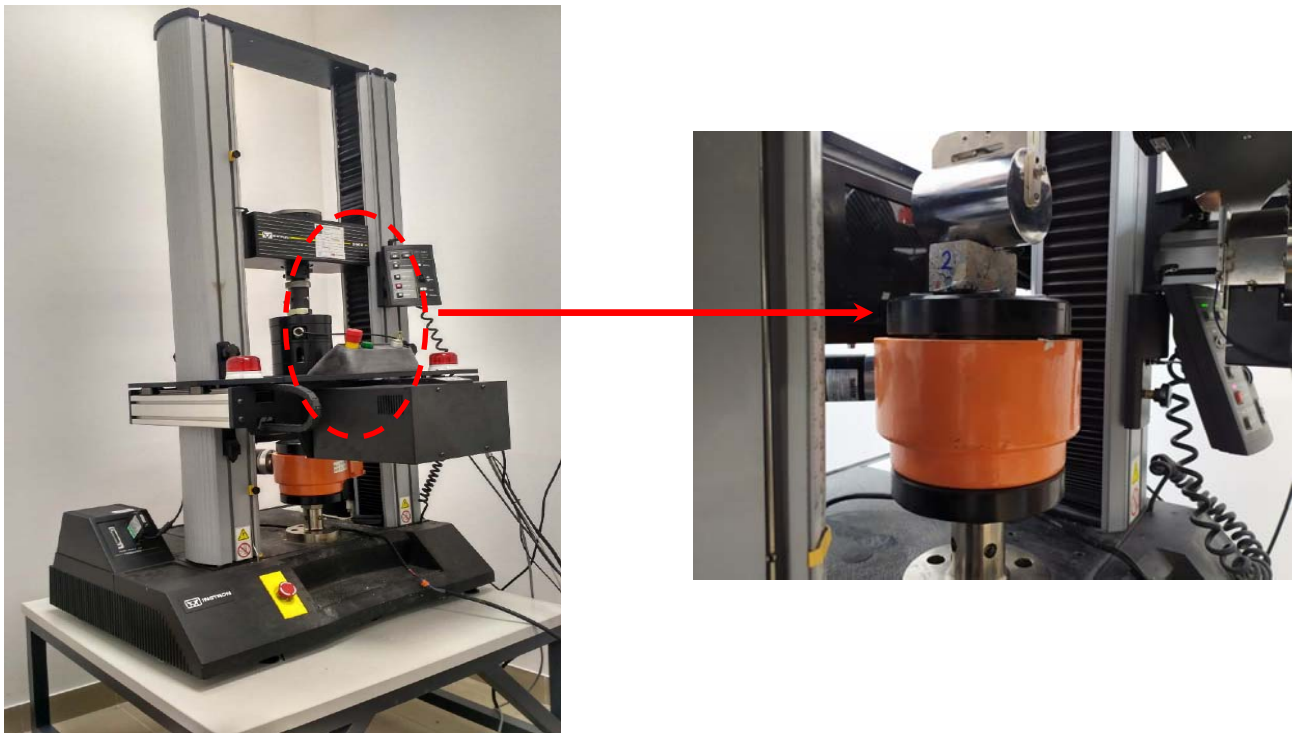

Figure 5: General view on X-ray micro-CT system Skyscan 1173 mounted on loading machine Instron 5569 and zoom on short reinforced concrete beam mounted on rotation table in horizontal position

FIGURE 5

a) b)

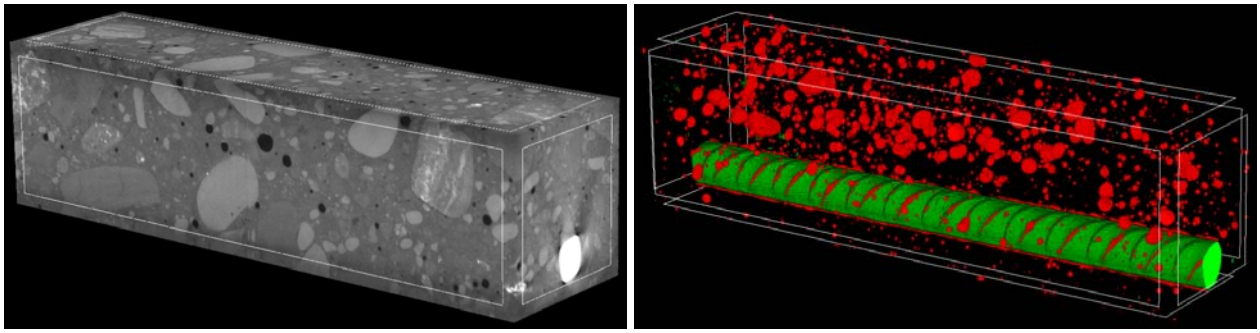

A)

a) b)

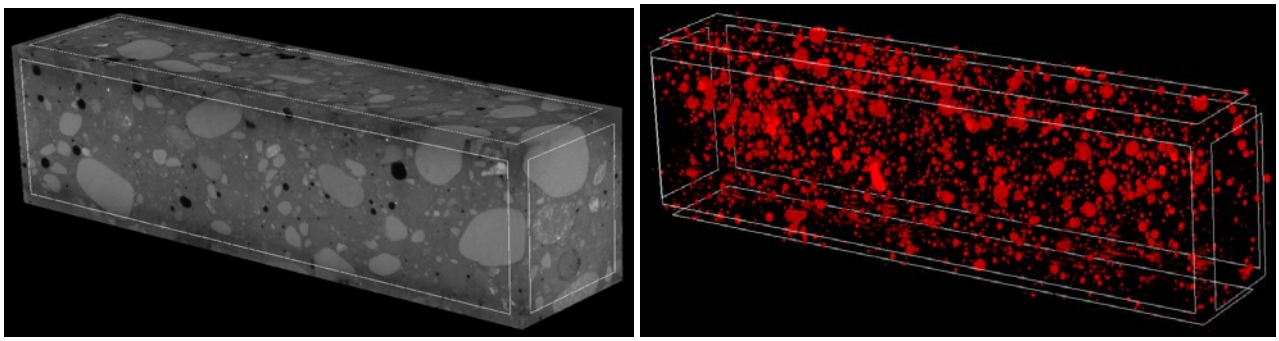

B)

Figure 6: Initial view on beams a) and distribution of pores in 3D micro-CT images b) of non-cracked long RC beams (L=160 mm) before loading: A) with steel bar and B) with basal bar

FIGURE 6

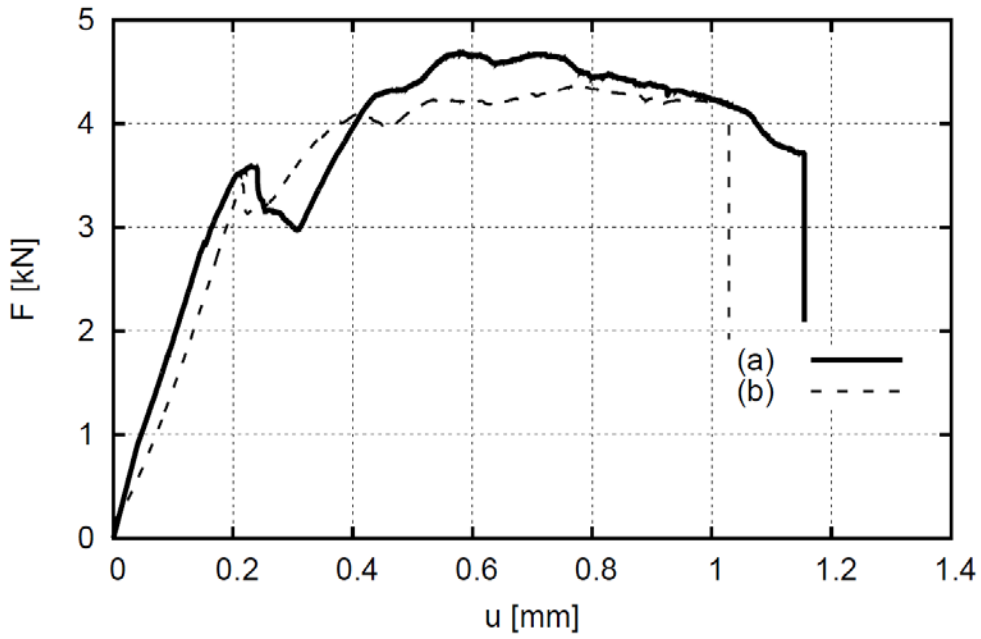

Figure 7: Experimental vertical force F - deflection u diagrams for long RC beams (L=160 mm) with: a) steel and b) basalt bar

FIGURE 7

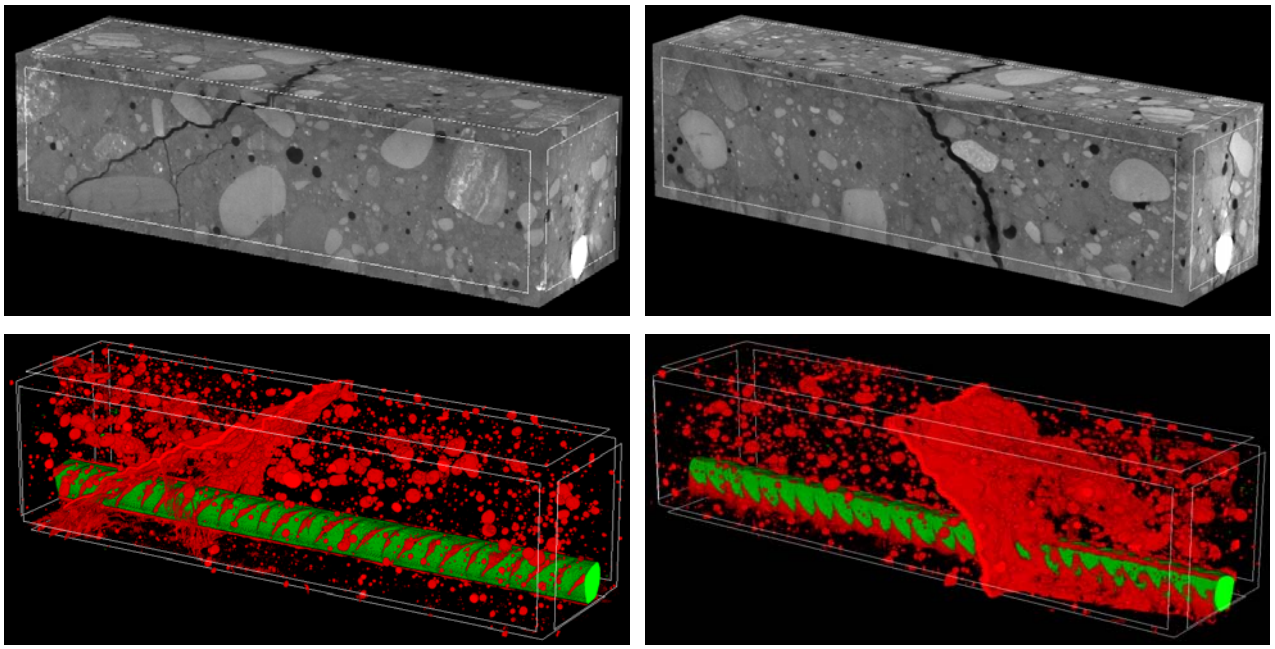

A)

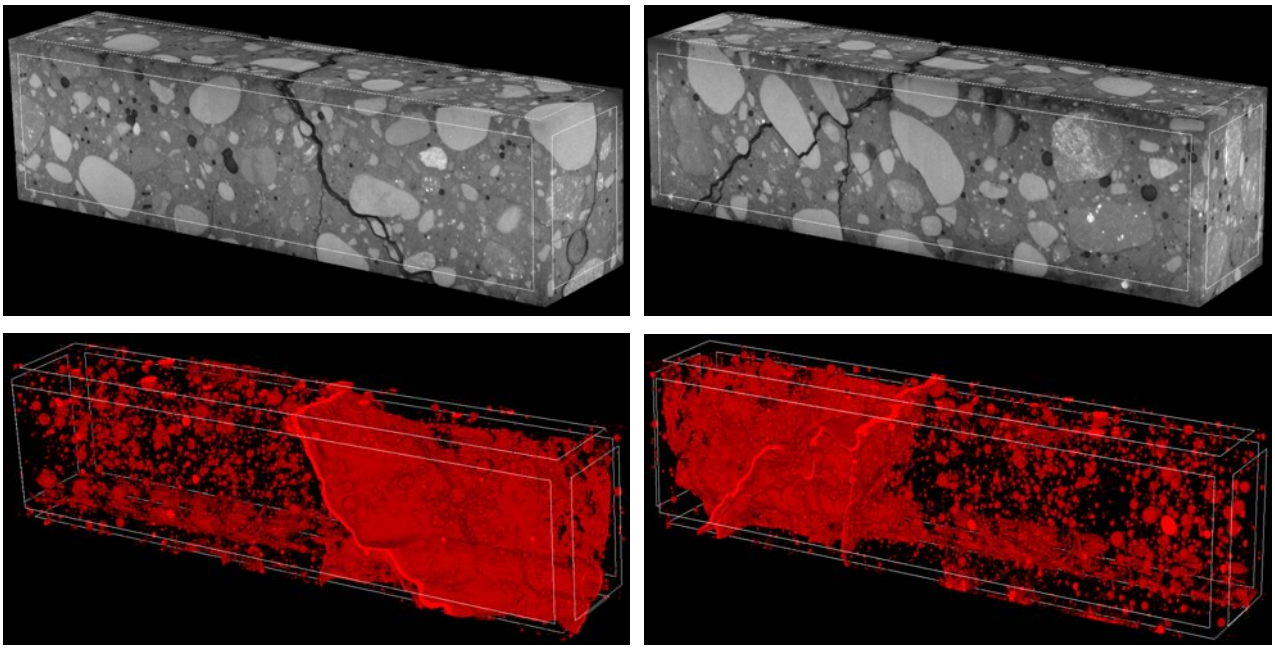

B)

Figure 8: Final 3D micro-CT images on 2 sides of long cracked concrete beams (L=160 mm) reinforced with: A) steel bar and (B) basalt bar for deflection about u=1.0 mm (a) beam front side and b) beam rear side, pores and cracks are in red, steel bar is in green)

FIGURE 8

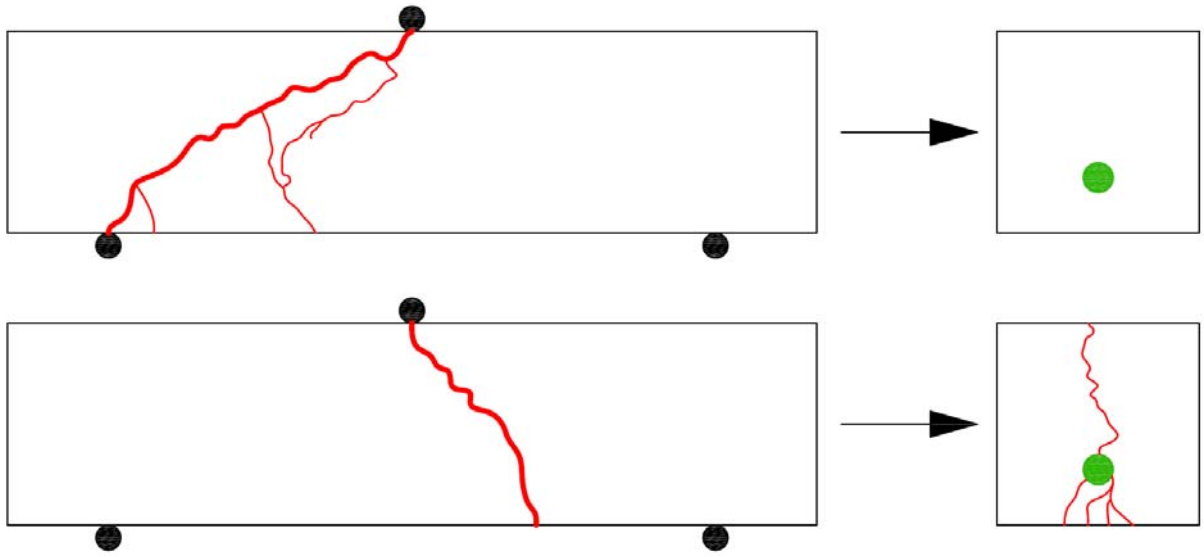

a)

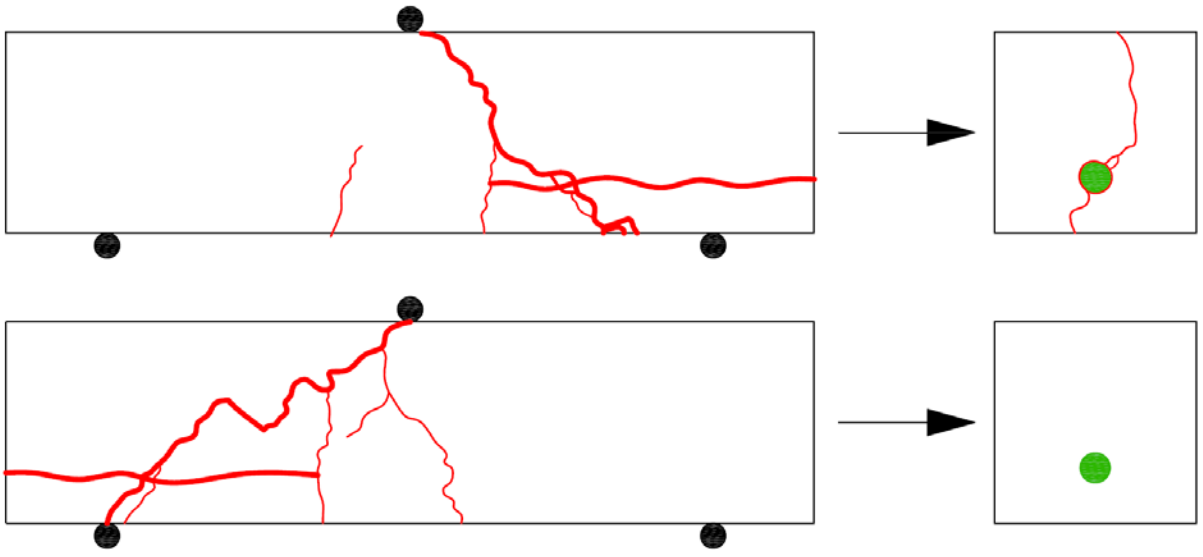

b)

Figure 9: Sketch of final crack pattern in long RC beams (L=160 mm) on all sides with: a) steel bar and b) basalt bar (cracks are marked in red, critical shear crack is marked as thick red line, reinforcement bar is marked in green)

FIGURE 9

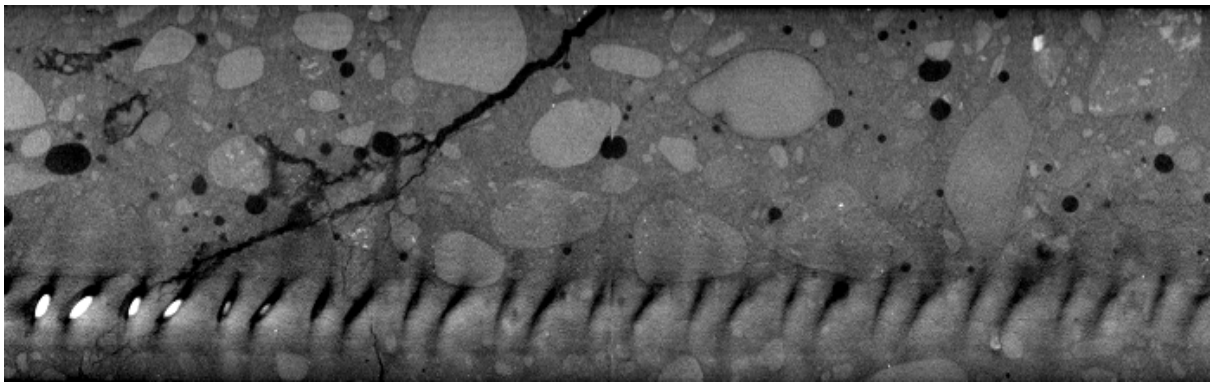

a)

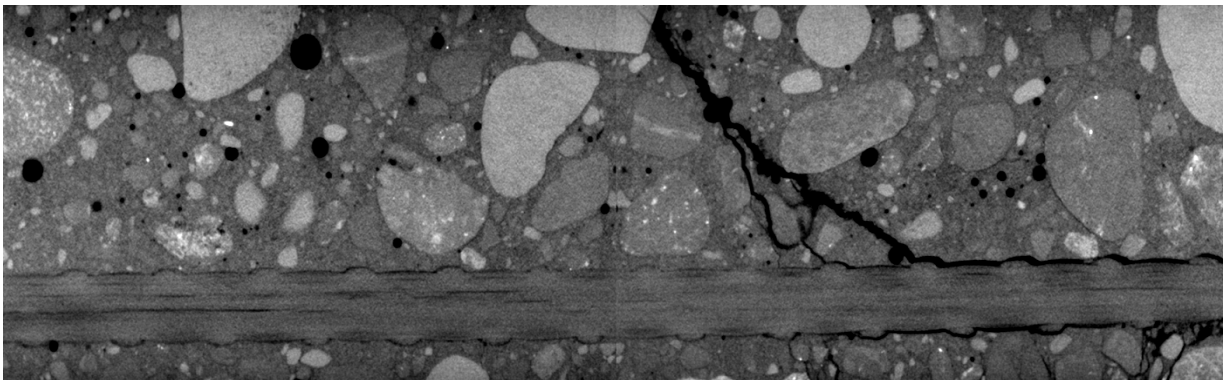

b)

Figure 10: Vertical cross-section at mid-width of long RC beam (L=160 mm) with: a) steel bar and b) basalt bar

FIGURE 10

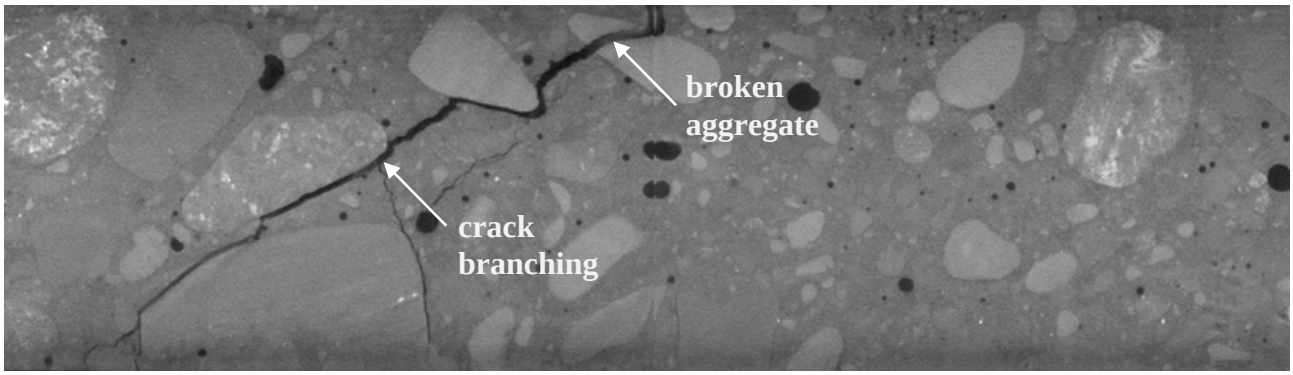

a)

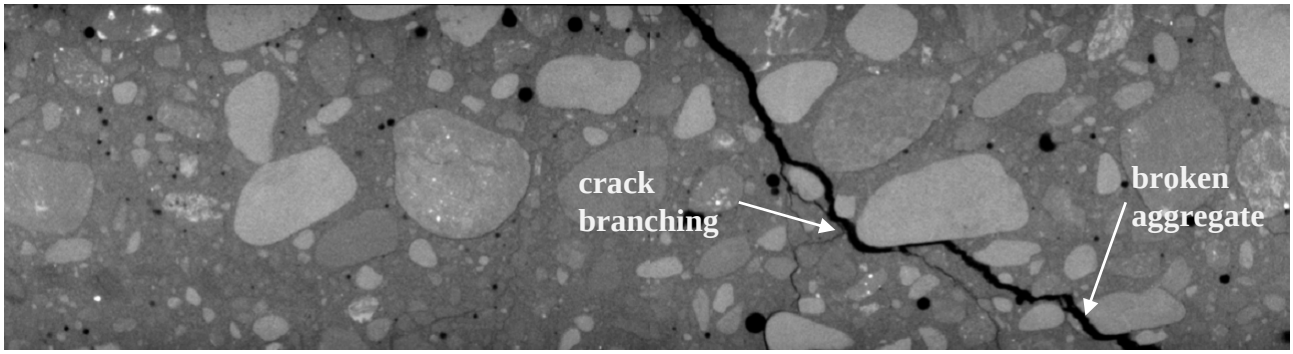

b)

Figure 11: Crack crossing weak aggregate and crack branching in long RC beam (L=160 mm) with: a) steel bar and b) basalt bar

FIGURE 11

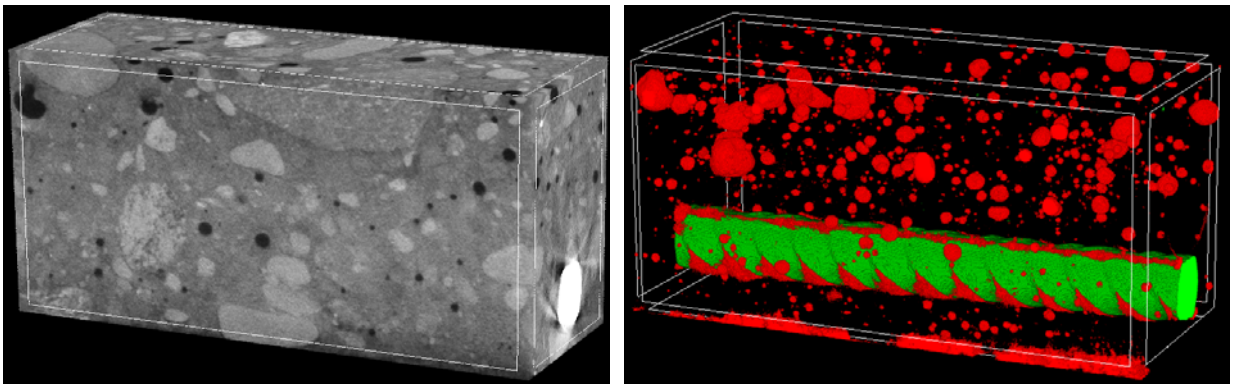

a)

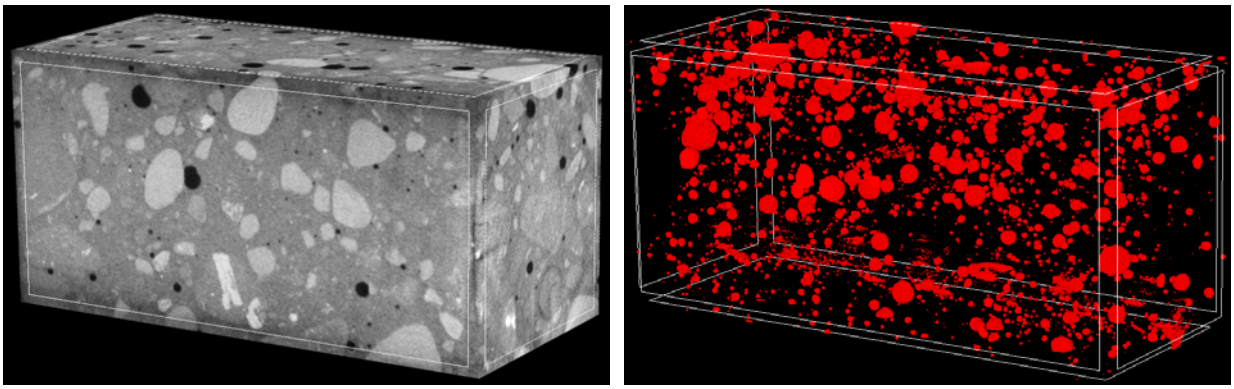

b)

Figure 12: General view on beams and distribution of pores in 3D micro-CT images of non-cracked short RC beams (L=80 mm) before loading reinforced with: a) steel bar and b) basal bar

FIGURE 12

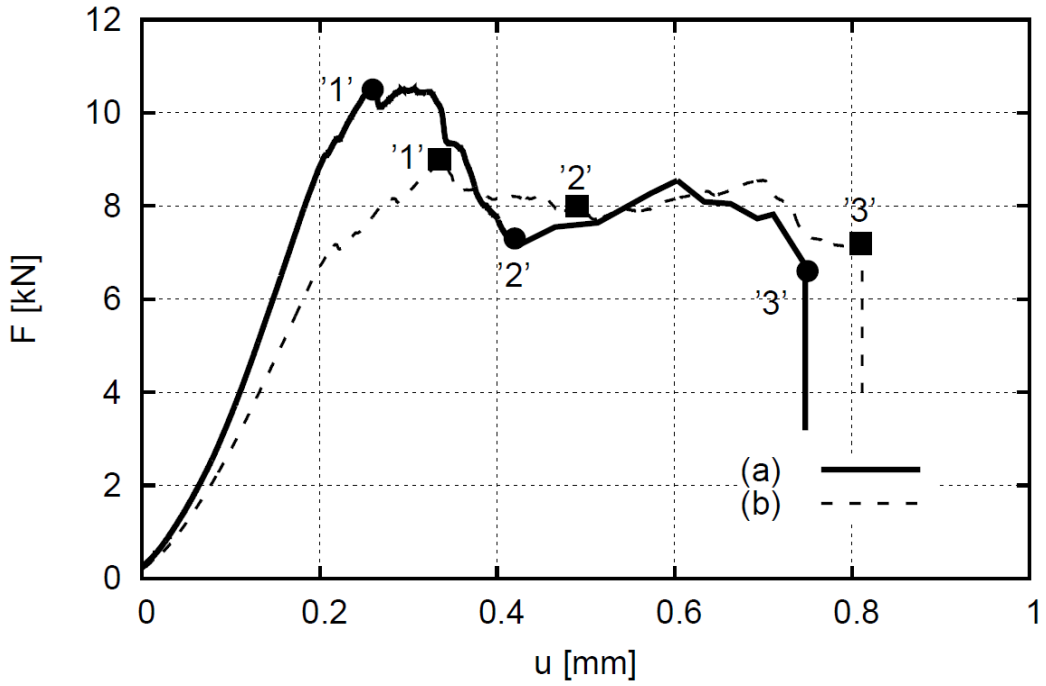

Figure 13: Experimental force (*F*) deflection *(u)* curve for short RC beams (*L*=80 mm) with: a) steel bar and b) basalt bar and marked micro-CT scanning points '1'-'3'

FIGURE 13

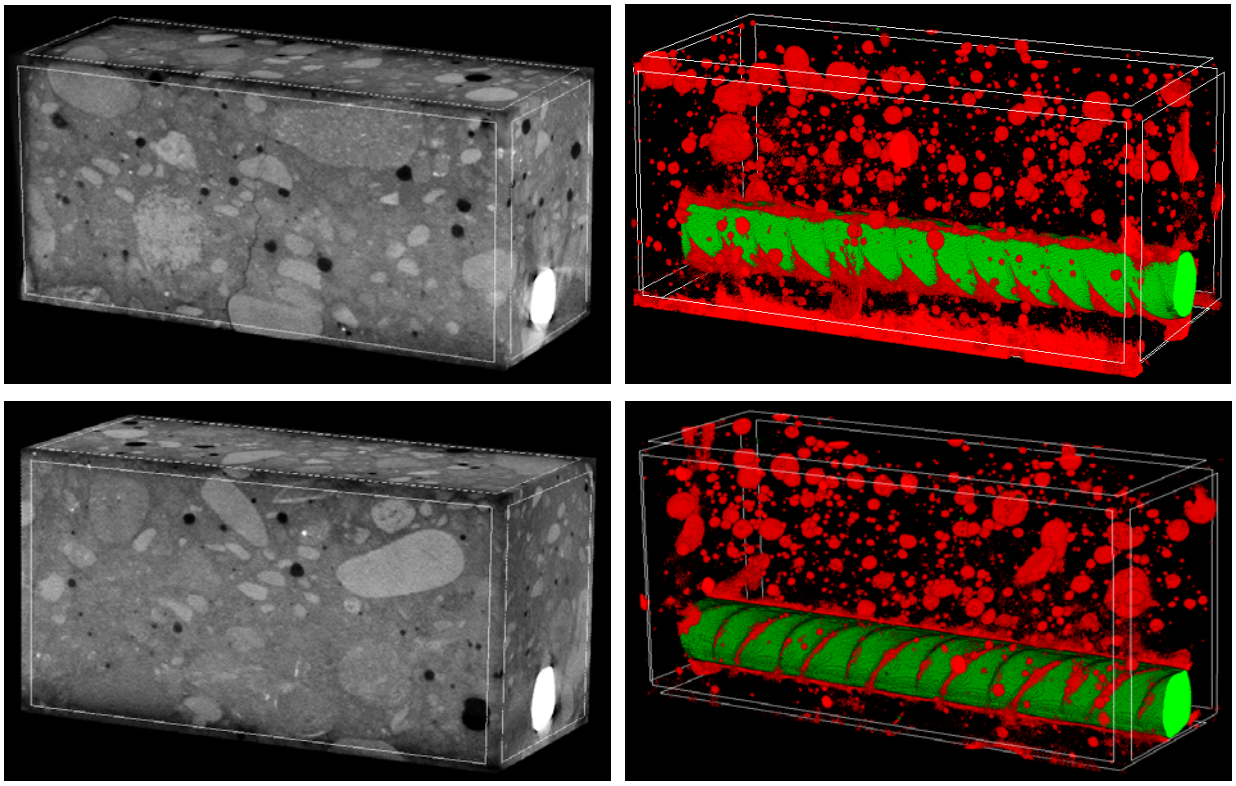

a)

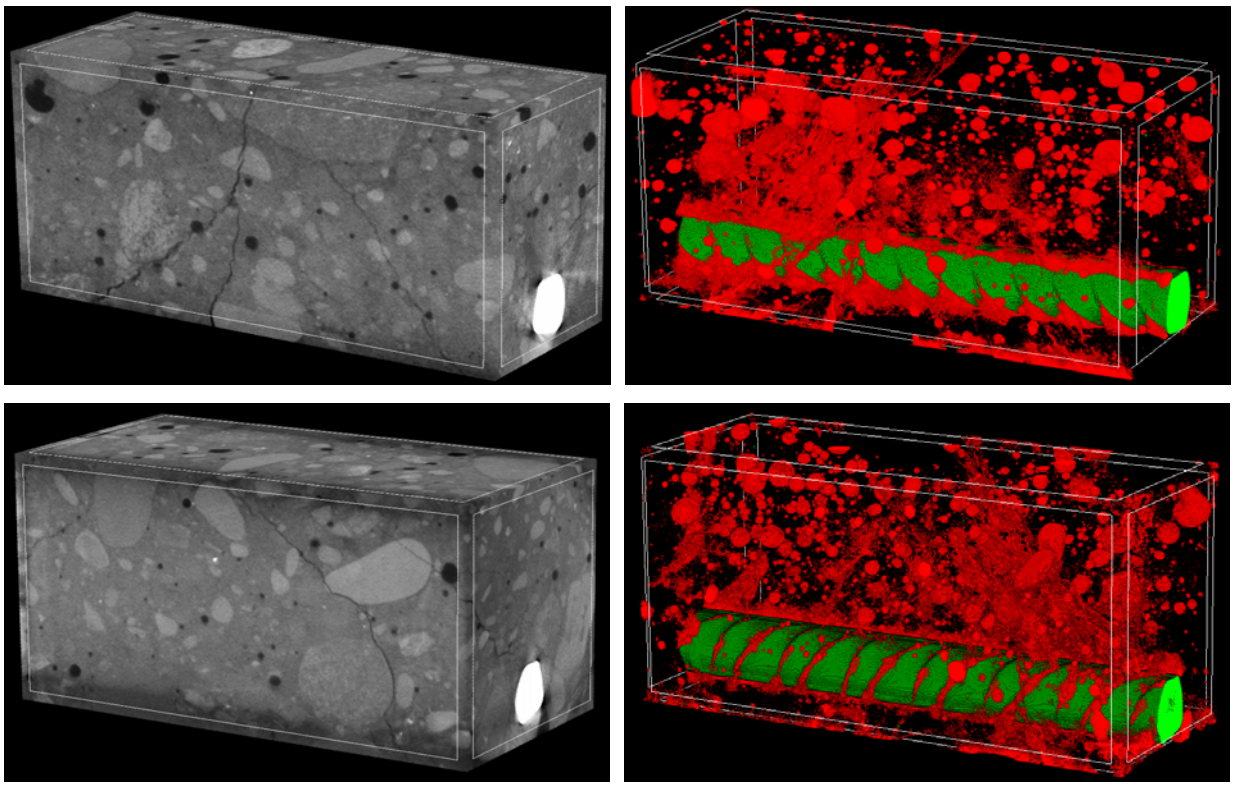

b)

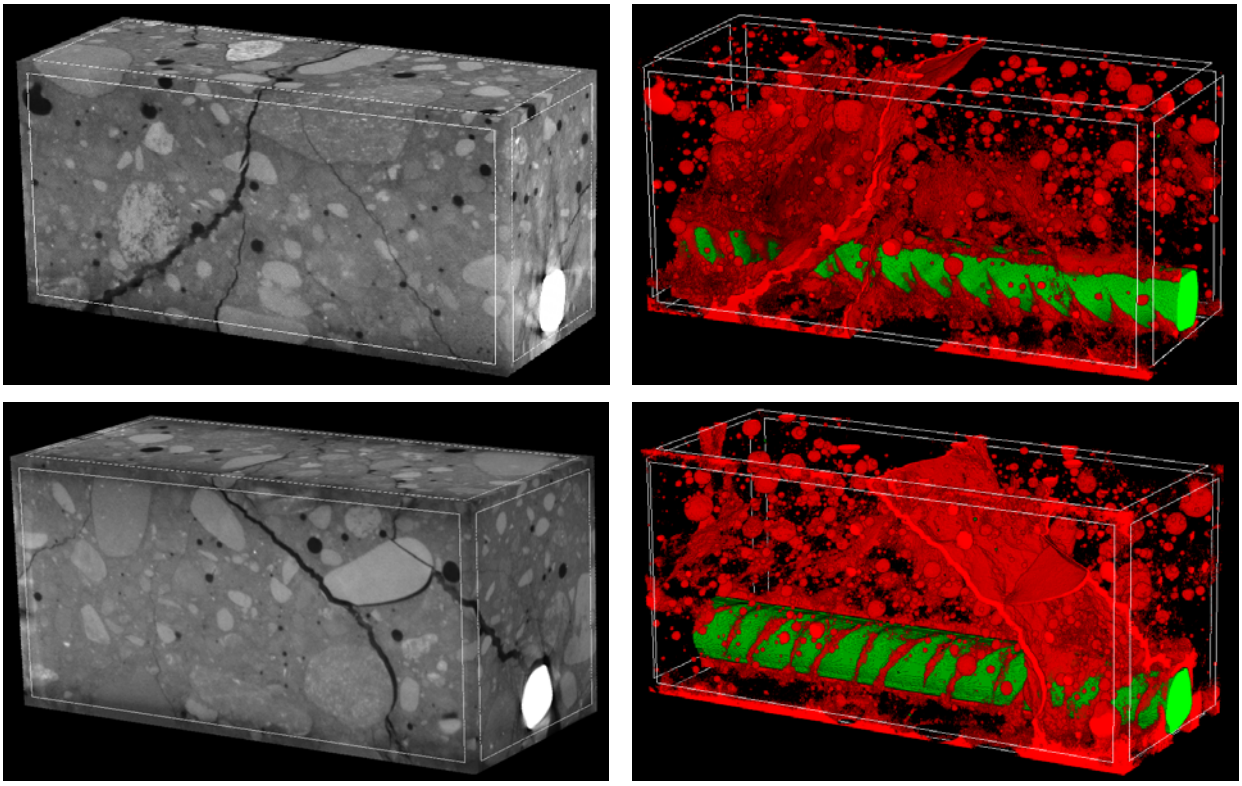

c)

Figure 14: 3D micro-CT images of short RC beam reinforced with steel bar (L=80 mm) on both sides for: a) point '1', b) point '2' and c) point '3' on curve F=f(u) of Figure 13 (pores and cracks are in red, steel bar is in green)

FIGURE 14

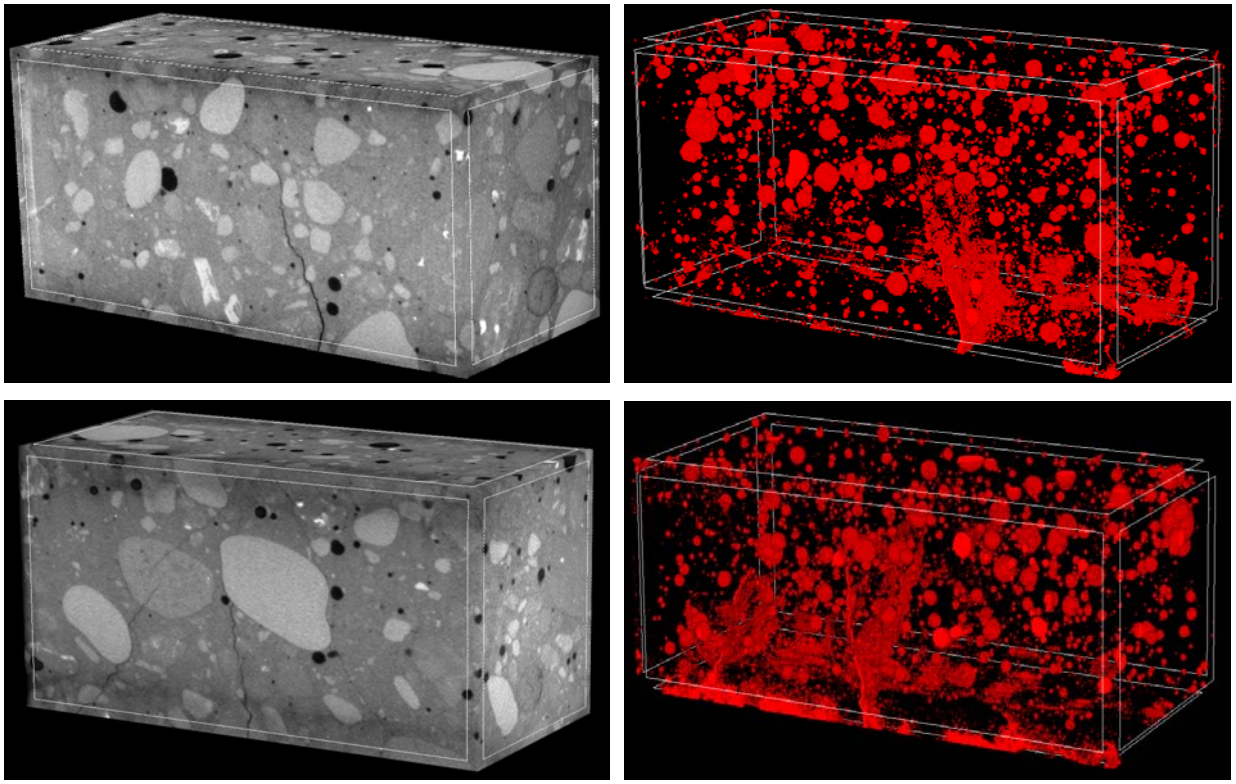

a)

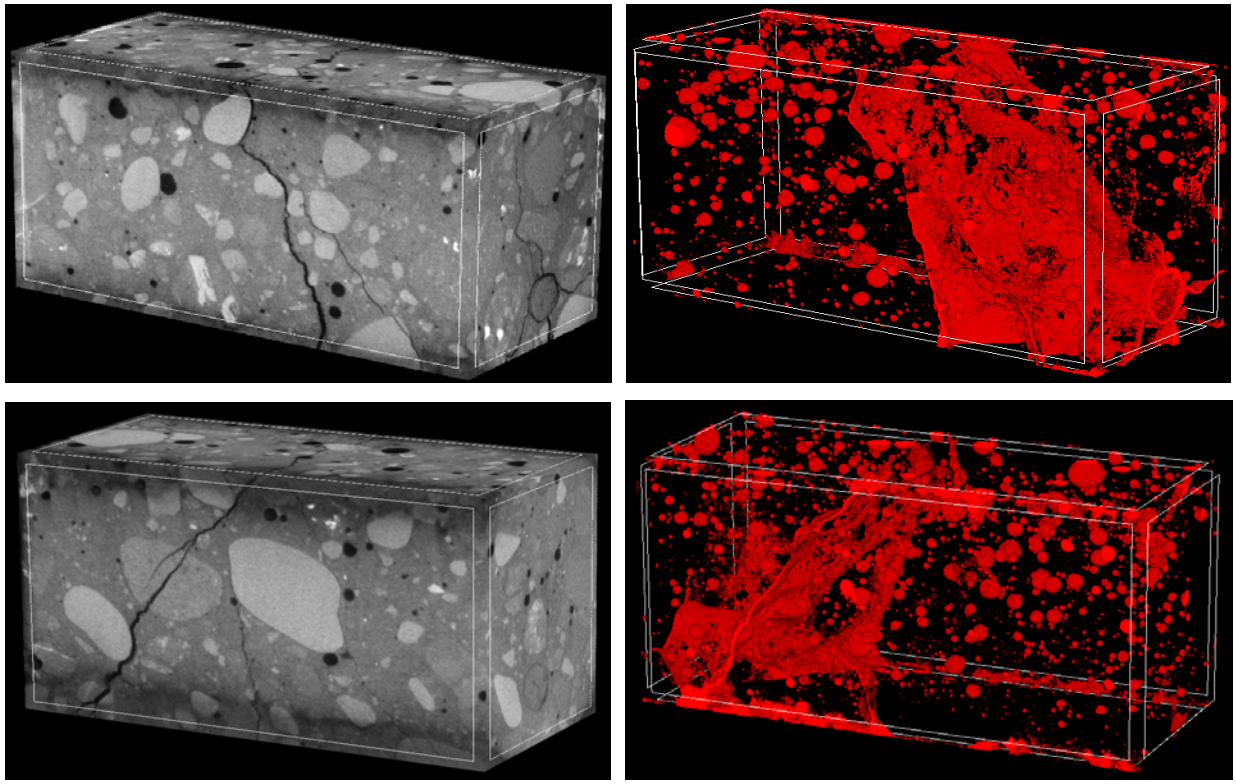

b)

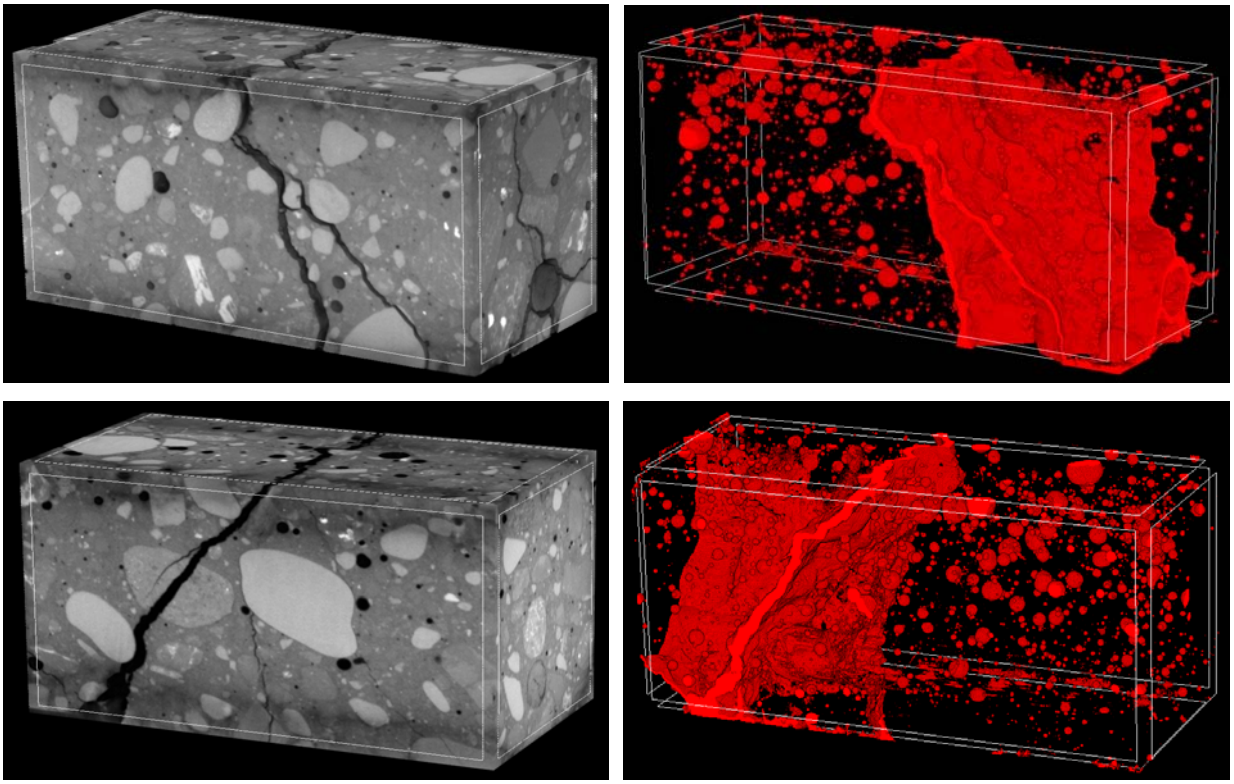

c)

Figure 15: 3D micro-CT images of short RC beam reinforced with basalt bar (L=80 mm) on both sides for: a) point ‘1’, b) point ‘2’ and c) point ‘3’ on curve F=f(u) of Figure 13 (pores and cracks are in red, steel bar is in green)

FIGURE 15

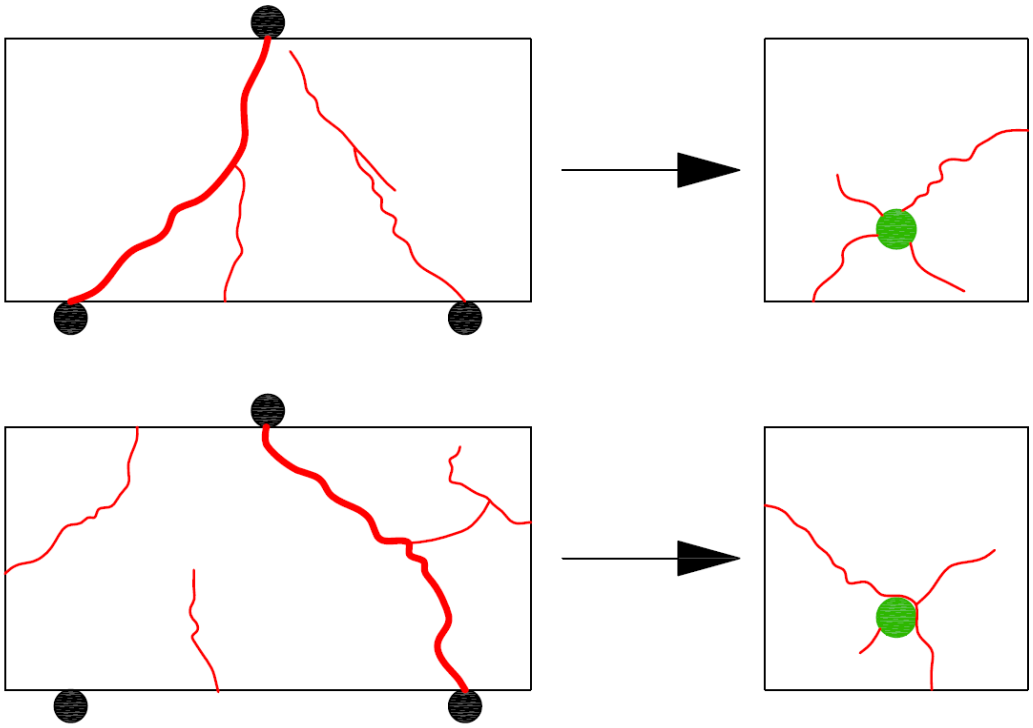

a)

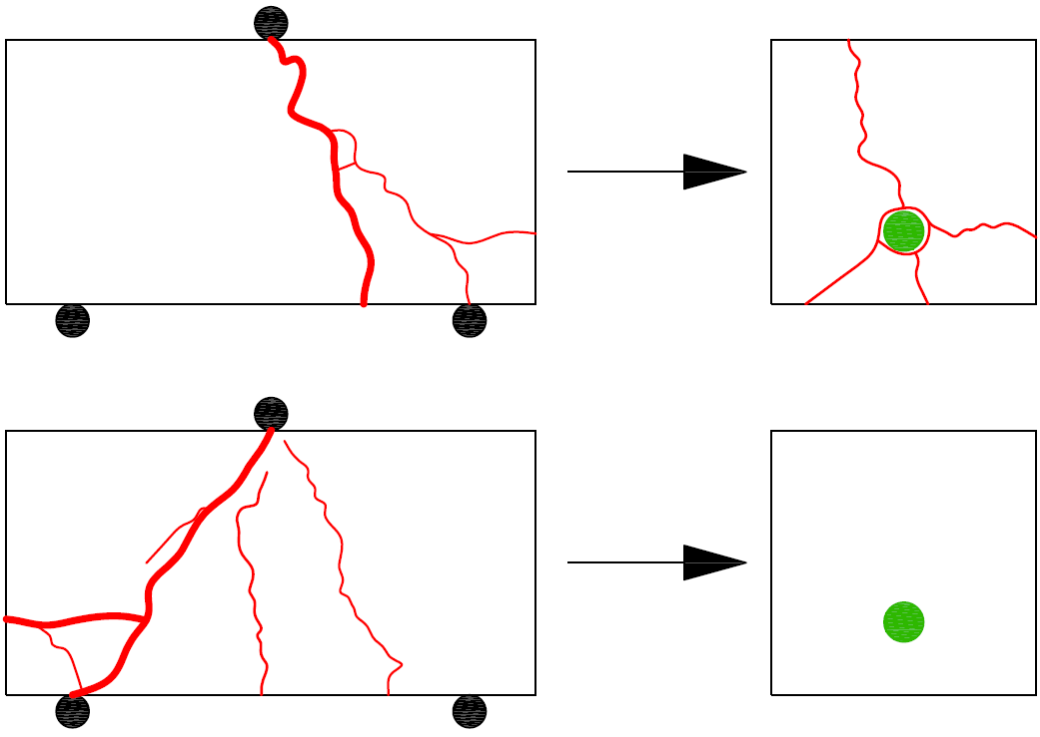

b)

Figure 16: Sketch of final crack pattern for short RC beams (L=80 mm) on all sides with: a) steel bar and b) basalt bar (failure crack is marked as thick red line, reinforcement is marked in green)

FIGURE 16

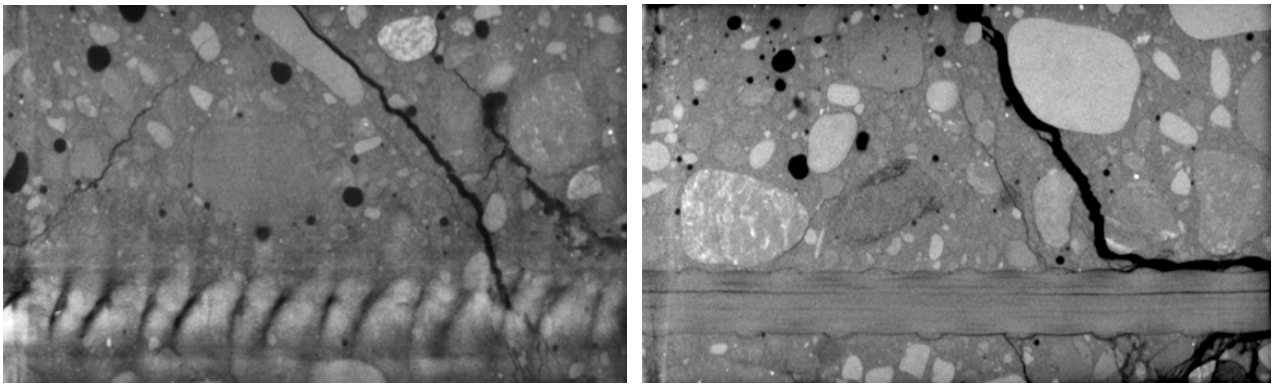

a) b)

Figure 17: Vertical cross-section at mid-width of short RC beam (L=80 mm) with: a) steel bar and b) basalt bar

FIGURE 17

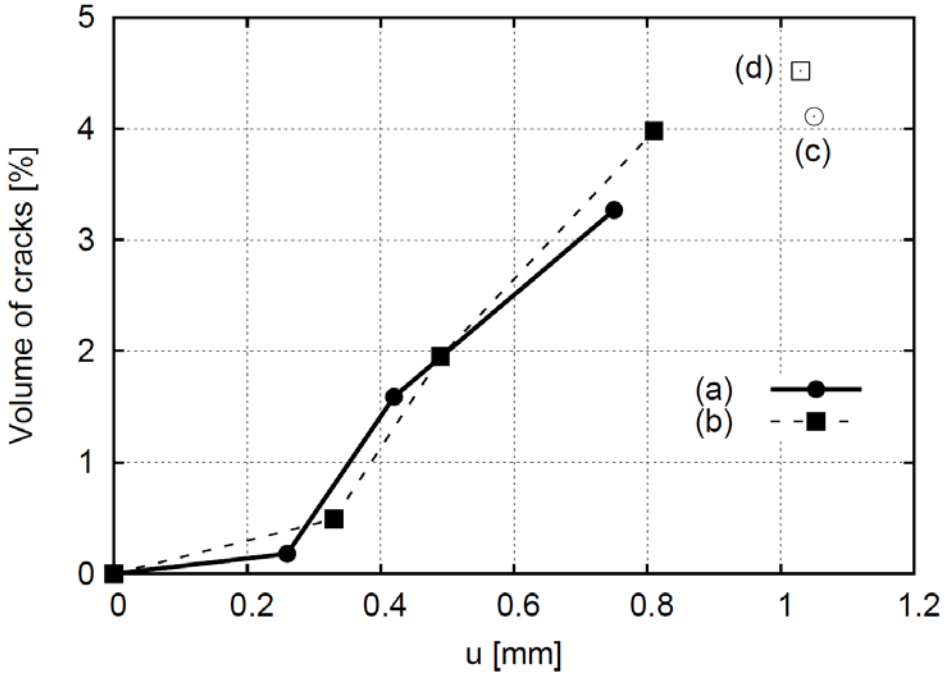

Figure 18: Relationship between volume of cracks and deflection *u* during bending for RC beams: a) short beam with steel bar (*L*=80 mm), b) short beam with basalt bar (*L*=80 mm), c) long beam with steel bar (*L*=160 mm) and d) long beam with basalt bar (*L*=160 mm)

FIGURE 18

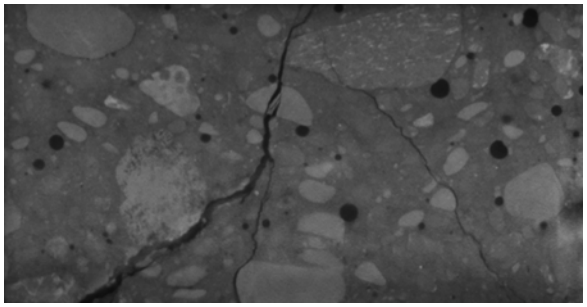

a)

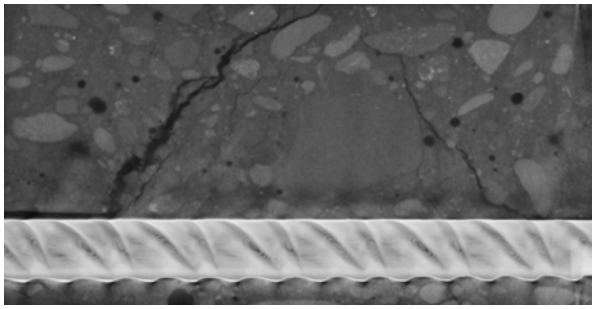

b)

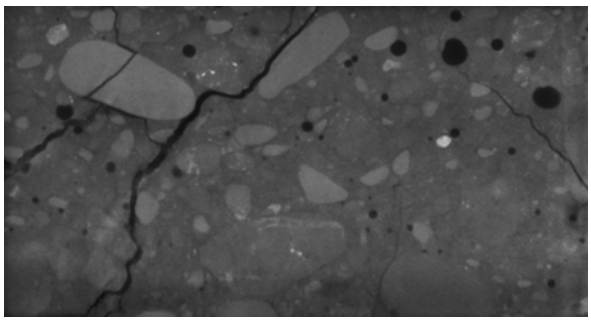

c)

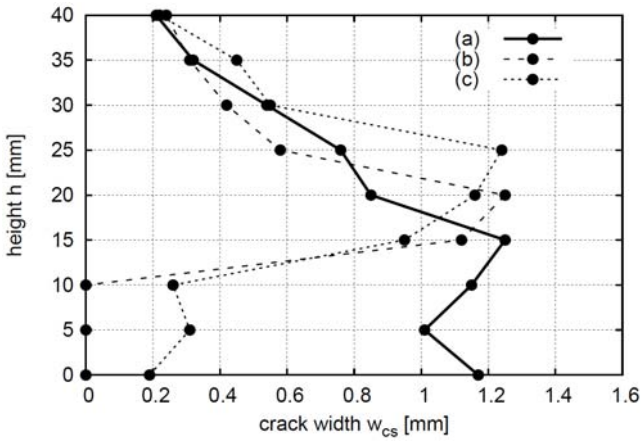

d)

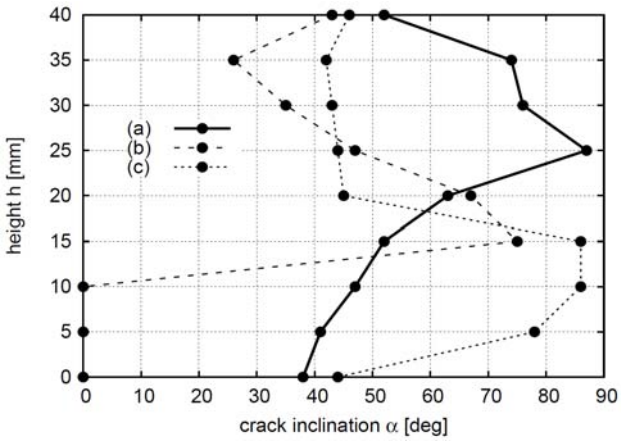

e)

Figure 19: Vertical cross-sections of short RC beam (L=80 mm) with steel reinforcement: a) at 5 mm from front side, b) at beam mid-width and c) at 5 mm from rear side and corresponding measurement results of critical shear crack: d) crack width and e) crack inclination angle

FIGURE 19

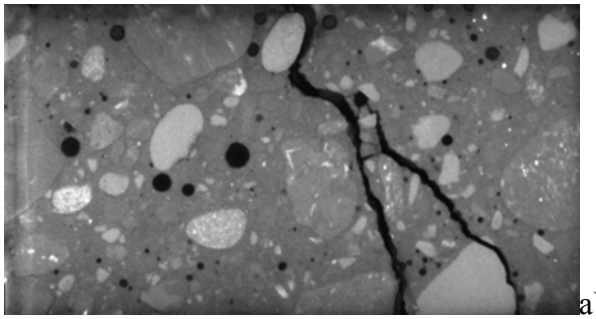

a)

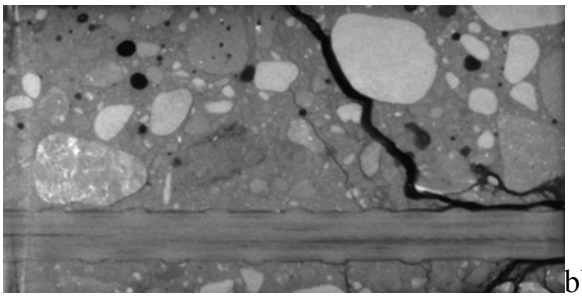

b)

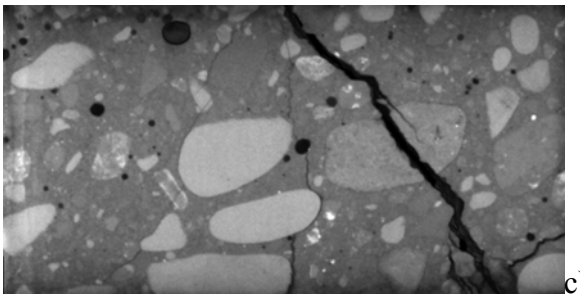

c)

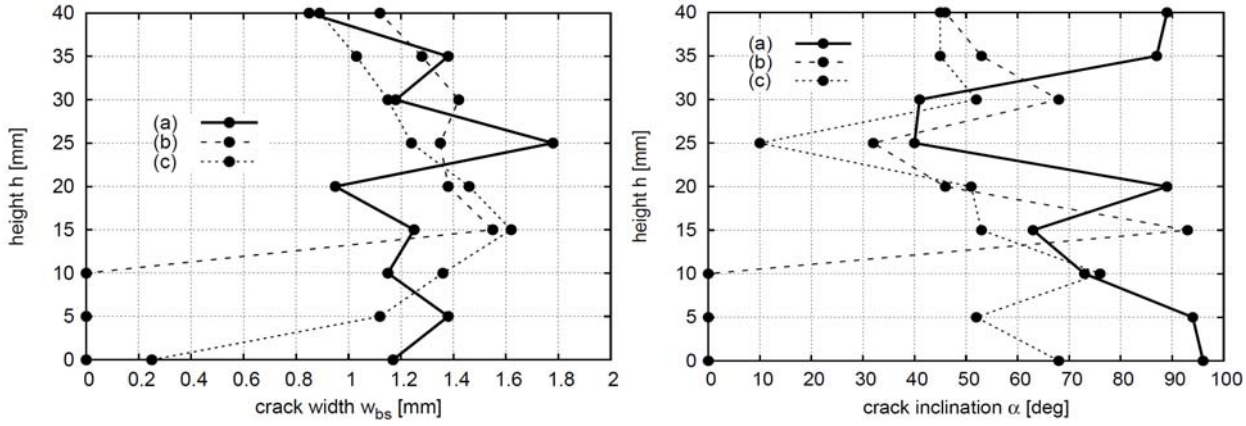

d) e)

Figure 20: Vertical cross-sections of short RC beam (L=80 mm) with basalt reinforcement: a) at 5 mm from front side, b) at mid-width and c) at 5 mm from rear side and corresponding measurement results of critical shear crack: e) crack width and f) crack inclination angle

FIGURE 20

LIST OF TABLES

Table 1: Concrete mix components (d_{50} – mean particle diameter, d_{max} – maximum aggregate diameter, d - particle diameter)

Concrete components	Volumetric mass of concrete components (d_{50}=2 mm and d_{max}=16 mm)
Cement CEM II 32 .5R	360 kg/m^3
Sand (d=0-2 mm)	650 kg/m^3
Gravel aggregate (d=2-8 mm)	580 kg/m^3
Gravel aggregate (d=8-16 mm)	580 kg/m^3
Superplasticizer	1.8 kg/m^3
Water	150 kg/m^3

Table 2: Volume of pores, cracks and maximum crack width in long RC beams (L=160 mm) measured by 3D micro-computed tomography at initial and final state

RC beam	Initial volume of pores [%]	Initial volume of closed pores [%]	Initial volume of open pores [%]	Final volume of pores [%]	Volume of cracks [%]	Maximum crack width [mm]
With steel bar	2.64	2.14	0.50	6.75	4.11	1.39
With basalt bar	3.04	2.42	0.62	7.63	4.52	1.68

Table 3: Volume of initial pores in short RC beams (L=80 mm) measured by 3D micro-computed tomography

RC beam	Initial volume of pores [%]	Initial volume of closed pores [%]	Initial volume of open pores [%]
With steel bar	2.67	2.04	0.63
With basalt bar	2.83	2.24	0.59

Table 4: Volume of pores, cracks and maximum crack width in short RC beam (L=80 mm) with steel reinforcement measured by 3D micro-computed tomography at different loading steps

Loading point on curve F-u (Figure 13)	Force F [kN]	Deflection u [mm]	Volume of pores and cracks [%]	Volume of cracks [%]	Maximum crack width [mm]
Point '1'	10.46	0.26	2.85	0.18	0.16
Point '2'	7.33	0.42	4.26	1.59	0.48
Point '3'	6.49	0.75	5.94	3.27	1.25

Table 5: Volume of pores, cracks and maximum crack width in short RC beam (L=80 mm) with basalt reinforcement measured by 3D micro-computed tomography at different loading steps

Loading point on curve *F-u* (Figure 13)	**Force *F* [kN]**	**Deflection *u* [mm]**	**Final volume of pores and cracks [%]**	**Volume of cracks [%]**	**Maximum crack width [mm]**
Point '1'	9.05	0.33	3.32	0.49	0.27
Point '2'	7.98	0.49	4.78	1.95	0.72
Point '3'	7.21	0.81	6.81	3.98	1.78